Unravelling the Contribution of Kinetics and Mass Transport Phenomena to Impedance Spectra in Vanadium Redox Flow Batteries: Development and Validation of a 1D Physics-Based Analytical Model

Journal of The Electrochemical Society, 2020 **167** 110534

Unravelling the Contribution of Kinetics and Mass Transport Phenomena to Impedance Spectra in Vanadium Redox Flow Batteries: Development and Validation of a 1D Physics-Based Analytical Model

Daniele Vivona,* Mirko Messaggi,*,z Andrea Baricci, Andrea Casalegno, and Matteo Zago****

Politecnico di Milano, Department of Energy, 20156 Milano, Italy

Vanadium redox flow battery technology can support the spread of energy storage in stationary applications and allow higher penetration of renewables in the electric grid. Currently, its market competitiveness is hindered by low power density, which stems from complex interplay between kinetic and mass transport losses. The quantitative interpretation of experimental observations should rely on physics-based models, which allow a consistent comparison of different operative conditions. In this work, a fast analytical physics-based 1D model of the impedance of vanadium flow battery is presented and validated with respect to experimental data. The model, made available online at http://mrtfuelcell.polimi.it, employs a macro-homogeneous approach and considers losses due to kinetics, reactant distribution within the electrode (Sigracet® SGL 39 AA carbon paper), convection in flow channel and vanadium transport to electrode surface. Additionally, analytical expressions of contributions to impedance of single physical phenomena are derived through an asymptotical analysis. The results show that, at negative electrode, transport of ions to active surface is the limiting phenomenon at lower flow rates, while at higher flow rates depletion of reactants within electrode becomes critical together with charge transfer processes. At positive electrode, the main contribution to performance loss is the vanadium transport to electrode surface.

 [DOI: 10.1149/1945-7111/aba36b]

Manuscript submitted April 20, 2020; revised manuscript received June 11, 2020. Published July 17, 2020.

Flow battery technology is one of the best candidates to support the spread of electrochemical energy storage in stationary applications. Storing energy in a liquid electrolyte, which is maintained in external tanks and recirculated, guarantees safe operation and allows the independent design of energy capacity and power rating. Flow batteries base their operation on the valence shift of a metal ion and a variety of redox couples are under study.[1] Above all, vanadium redox flow batteries (VRFBs) are the most successful and already present in market applications.[2] Their main advantage consists in employing four oxidation states of a single chemical species, which is dissolved in both negative electrolyte (anolyte solution) and positive electrolyte (catholyte solution). Specifically, the ion couple V^{2+}/V^{3+} and VO^{2+}/VO_2^{+} are present at the negative and positive electrode, respectively. This characteristic solve irreversible cross contamination between the two electrodes with beneficial effects on limiting capacity reduction and achieving longer lifespans.[3] Currently, one of the major issues hindering the spread of VRFB technology in market applications is a low power density, which requires high installed active areas and thus high investment costs.[4,5] Despite zero gap architecture has provided great advancement towards an increased power density,[6] further improvements are still necessary. In particular, improving the understanding of how physicochemical phenomena governing battery operation translate into performance losses is crucial to support the design of optimized components and architectures, which can be employed in next generation of VRFB.[3] The operation of VRFB is regulated by a complex interplay of kinetic and mass transport phenomena occurring at different scales, which in absence of ad hoc diagnosis tools, makes difficult to evaluate techno-economic tradeoffs in the design phase.

Electrochemical impedance spectroscopy (EIS) is a widely used in situ characterization technique for the diagnose of different causes of voltage losses[7] in electrochemical devices. Through the application of a sinusoidal current or voltage perturbation, different physical phenomena occurring in the device are separated depending on their characteristic frequency.[8] Thus, EIS can in principle provide quantitative information on which particular physical phenomena limit VRFB performance. EIS experiments for flow batteries are complicated by a variation of state of charge (SoC) during battery operation, resulting in a not steady-state system operation. Such difficulty is overcome in research using the symmetric cell configuration - a useful tool for studying the behavior of each electrode in a separate way, avoiding SoC variations.[9] EIS on a symmetric cell has already been used in literature to study transport losses,[10] the effect of diffusion processes and electrode material[11] or variable electrode thickness and flow rate.[12]

Moreover, consistent and transferrable interpretation of experimental data is still not possible due to lack of appropriate models. The current tendency in flow battery-related literature is to use equivalent circuit methods (ECM),[10–14] which are able to provide only qualitative information when analyzing spectra at changing operative conditions. ECM postulate a representation of the electrochemical device in terms of electric impedances, before linking them to a direct physical phenomenon.[15–17] Oppositely, physics-based models are derived starting from governing equations and rigorously account for physicochemical phenomena occurring in the device. In the literature limited effort has been dedicated to the development of physics-based models. Zago et al.[18] developed a 1D numerical impedance model of the negative electrode of a VRFB starting from governing equations of the different mass transport mechanisms in the porous electrode. The approach permits to highlight the sources of the different impedance features and points out the relevant contribution of convection at carbon fiber and transport of reactants to the active surface of porous electrodes. Due to the complex interplay of different phenomena and the importance of fluid dynamics in the real operation, the simple model showed limited agreement with the experimental data. Sun et al.[12] developed a 1D numerical model as a tool to separate and evaluate ohmic, charge transfer and diffusion overpotentials from experimentally measured EIS at different flow rates and with different electrode thicknesses. With the analysis of the recorded spectra, they quantified the

*Electrochemical Society Student Member.
**Electrochemical Society Member.
zE-mail: mirko.messaggi@polimi.it

decrease in the overpotentials related to ohmic and charge transfer losses caused by a greater thickness of the electrode and the reduction of the diffusive losses caused by a raise of the flow rate. More complex 3D numerical model coupling fluid dynamics and electrochemistry can be found in literature, such as those developed by Xu et al.,[19] Al-Yasiri et al.[20] and Messaggi et al.[21] These models employ computational fluid dynamics to couple complex mass transport phenomena with electrochemistry and solve for a 3D spatial distribution of the main quantities inside the electrode for real geometries of the flow field. Thus, they can be used to design novel geometries to improve reactants distribution. However, numerical models are usually complex and require high computational costs, making impossible high throughput interpretation of experimental impedance spectra. Experimental and numerical studies on innovative geometries are reported in Refs. 22–24. In Ref. 22 Lisboa et al. developed a corrugated flow field with the aid of a CFD model and tested it experimentally in order to enhance mass transport in a small scale VFRB. Comparing the results with the parallel flow field, the authors achieved a two-fold increase in net power density. Akuzum et al.[23] manufactured 3D-printed ramps and obstacles to be inserted in interdigitated and parallel channels to change channel depth and facilitate electrolyte permeation in the porous electrode. With this approach they achieve an increase in power density up to 15% with respect to standard flow fields, and a reduction of the pressure drop. Zeng et al.[24] proposed a hierarchical interdigitated flow field designed through a simplified flow resistance model aiming to the reduction of pressure drops. This allowed to raise the voltage efficiency of around 4% in a cell of 40 cm^2. These literature works highlight improvements in VRFB performance through design of novel flow field geometries, but the physical reasons behind the obtained improvements have not been investigated in depth and completely understood. Simplification of governing equations can lead to the development of valid analytical physics-based models, which allow fast processing of experimental data.[25–27] Furthermore, analytical physics-based models are useful to derive expressions of impedances directly related to single transport mechanisms. Extensive effort has already been dedicated to the development of analytical physics based impedance models for proton exchange membrane fuel cells (PEMFC), which has helped understanding their functioning and pointing out the major sources of loss.[28–32] Currently, literature lacks of analytical physics-based model for the impedance of vanadium flow batteries and lot of room for improvement is left in the interpretation of their EIS spectra. Research effort directed to analytically model physical phenomena occurring in VRFB can pave the way to advanced engineering of such devices.

In this manuscript, a fully analytical 1D model for the impedance of a VRFB electrode is presented. Electrochemical reactions are described with Butler Volmer kinetics and mass transport is solved in the through electrode direction, considering the channel-electrode interface as a convective mass transport resistance. Moreover, the model accounts for transport within the electrode pores from the bulk of electrolyte to the active surface of carbon fiber. The model is validated against experiments recorded on both positive and negative symmetric cell using a simple graphic-based fitting procedure. Furthermore, analytical expressions for impedances referred to single transport phenomena are obtained via asymptotical analysis and are used to evaluate causes of performance losses. Sensitivity analysis on model parameters is included in Appendix A. With the aim of accelerating the development of flow battery components and supporting transition towards low carbon energy, the model is made available online at http://mrtfuelcell.polimi.it.

Experimental

Experimental setup.—The experimental tests were performed using a symmetric cell configuration, which is a useful investigation tool that guarantees a constant SoC during the experiments.[11] The cell active area was square-shaped 25 cm^2 with in-house-manufactured single serpentine graphite distributors, characterized by 1 mm × 1 mm channel section and 1 mm rib thickness. The electrodes were Sigracet® SGL 39 AA carbon paper (nominal thickness of ∼290 μm, compressed to 230 μm) and the membrane was Nafion® 115 with a thickness of 127 μm. The cell temperature was maintained at ambient temperature of 23 ± 2 °C. The electrolyte solution was prepared mixing 223 g of vanadium IV sulphate oxide hydrate (Alfa Aesar) and 5 M sulfuric acid (Fischer Chemicals), to obtain 600 ml of a 1.6 M solution of vanadium ions. Subsequently, 200 ml of both positive and negative electrolyte were obtained following the charging procedure described in Ref. 33. The bottles containing the electrolyte were maintained pressurized with N_2 to avoid the intake of air. In the hydraulic circuit a pulse dampener[11,34] was introduced to get rid of flow rate fluctuations induced by the peristaltic pump (Watson-Marlow 323Du with a 314Dw 4 roller headpump). A potentiostat (Autolab PGSTAT 30®) equipped with a frequency response analyzer module was used to perform polarization curves and impedance spectra.

Experimental tests.—Polarization curves were performed in potentiostatic mode following a one-way curve and reducing the voltage by steps of 0.05 V, with each step being held for 120 s in order to reach a steady value of current. The voltage range was 0.5/−0.5 V for the positive symmetric cell and 0.35/−0.35 V for the negative symmetric cell, respectively. The voltage limits were chosen in order to avoid the occurrence of oxygen and hydrogen evolution. In the post processing of acquired raw data of current density, the initial transitory was excluded in each voltage step and the average value of the remaining data was considered. The investigated operating conditions for both negative and positive symmetric cell configuration were SoC 50% and 10 and 20 ml min^{-1} electrolyte flow rate.

The impedance spectra were measured in galvanostatic mode. The frequency range was 10 kHz to 10 mHz with a logarithmic distribution. The investigated current densities were 0.05 and 0.1 A cm^{-2} for the negative symmetric cell, while for the positive one 0.05 and 0.2 A cm^{-2}. Each test was performed at least twice to verify the repeatability of the measurement.

Model

A representation of the half-cell domain specifically focusing on the mass transfer of vanadium ions is depicted in Fig. 1, in which the x direction represents the through electrode coordinate. Impedances related to mass transport phenomena and causing voltage loss are shown as well.

At the channel/electrode interface a convective mass transport resistance models voltage loss related to concentration gradient between bulk of the channel and the electrode interface. Vanadium ions are transported within the electrode along the x-direction (purple arrow) and subsequent transport from the center of pores to the active surface of carbon fibers - where reaction takes place - occurs through an interfacial layer (red arrows). As a result, the vanadium ions encounter two additional impedances on their way to the reaction sites. The first one $Z_{\mathfrak{D}}$ refers to their transport along the x coordinate, while the second one Z_k is associated to the pore level transport and movement through the electrolyte/electrode interface. A detailed mathematical description of transport mechanisms will be given while introducing governing equations in the following.

Macro-homogeneous approach is used to describe the electrode, which is taken as a continuum with fixed transport properties.[35] Moreover, the model is based on the following hypotheses:

I. Proton conductivity of the electrolyte is very high and thus local perturbation in overpotential are small.[30]
II. Side reactions and crossover of vanadium ions through the membrane are neglected.
III. The total concentration of vanadium ions is constant in all the points of the domain.
IV. The domain is isothermal.

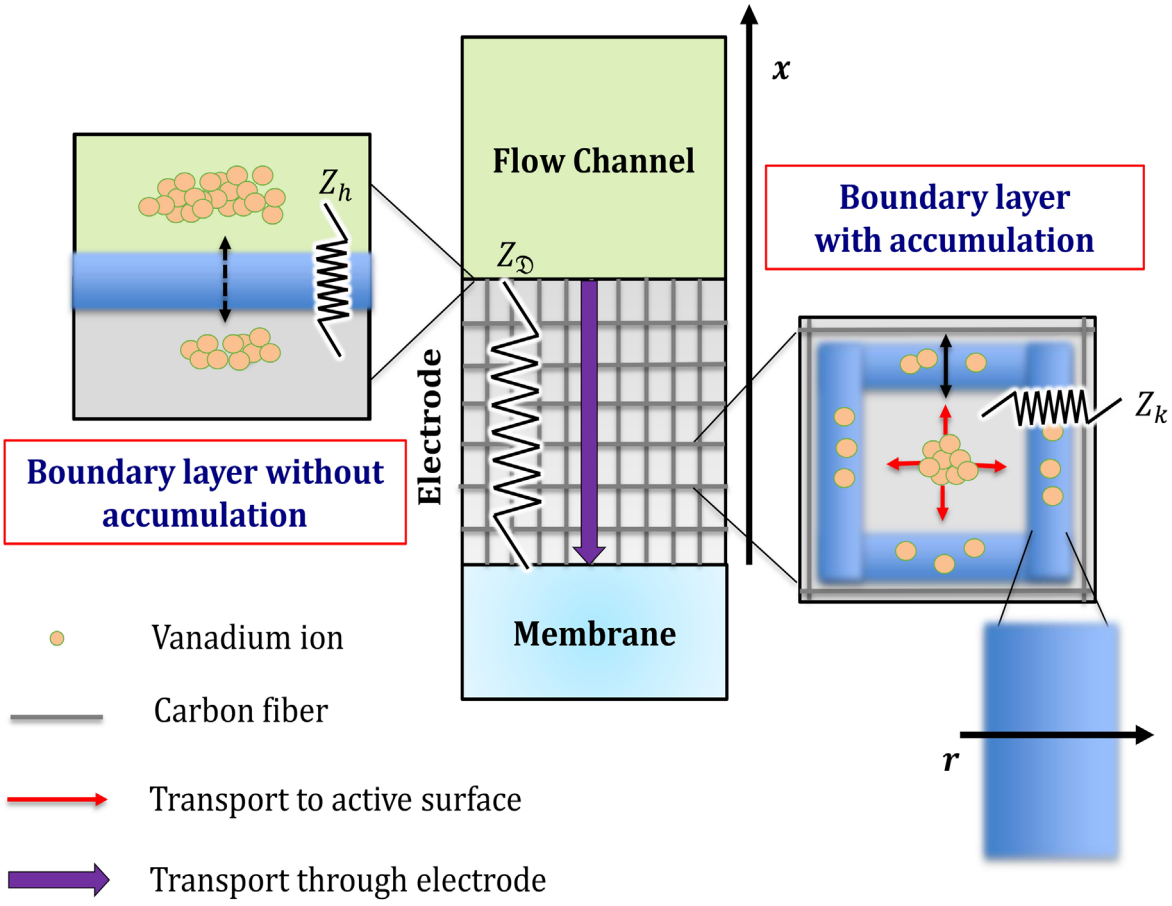

Figure 1. Schematic illustration of model domain (not to scale).

V. Migration is negligible. This assumption is often made in modelling-related literature.[36]
VI. The membrane is responsible for a purely ohmic effect considered constant for any value of current density.
VII. Homogeneity of all the quantities in the along-the-channel direction.

Variations of state of charge due to recirculation in tank reservoirs are neglected in this work because the model is validated against data recorded on a symmetric cell.[37] Moreover, activities of vanadium ions are taken equal to their concentrations in the electrolyte. This last hypothesis is valid when the electrolyte solution is highly diluted and is typically valid for flow batteries.[2]

DC model development.—Butler Volmer kinetics is used to describe the rate of reactions taking place in the VRFB electrode. Considering negative (positive) symmetric cell, V^{2+} (VO^{2+}) oxidation occurs at one electrode and V^{3+} (VO_2^+) reduction occurs at the other electrode: the corresponding reactions are reported in Eqs. 1 and 2.

$$V^{2+} \underset{oxi}{\overset{red}{\leftrightarrows}} V^{3+} + e^-, \; E^0 = -0.26 \text{ V} \;\; \text{vs SHE} \qquad [1]$$

$$VO_2^+ + 2H^+ + e^- \underset{red}{\overset{oxi}{\leftrightarrows}} VO^{2+} + H_2O, \; E^0 = +1.00 \text{ V} \;\; \text{vs SHE} \qquad [2]$$

In (1) and (2) E^0 is the reversible potential associated to the reaction, measured with respect to a standard reference electrode. Electrochemical reaction rates related to the reactions (1) and (2) are written according to Butler-Volmer in Eqs. 3 and 4 respectively, in which the concentrations of reactants and products appear with the subscript s, meaning that they are referred to their value on the active surface of the electrode.

$$r = a \; k_f c_{V^{2+},s} \; \exp\left(\frac{\Delta\phi}{b_f}\right) - a \; k_b c_{V^{3+},s} \; \exp\left(-\frac{\Delta\phi}{b_b}\right) \qquad [3]$$

$$r = a \; k_f c_{VO_2^+,s} \; \exp\left(\frac{\Delta\phi}{b_f}\right) - a \; k_b c_{VO^{2+},s} \; \exp\left(-\frac{\Delta\phi}{b_b}\right) \qquad [4]$$

In Eqs. 3 and 4 a is the specific surface area of the electrode, k_f and k_b are the kinetic rate constants of the forward and backward reaction, respectively; b_f and b_b are the corresponding Tafel slopes, which are computed as Eq. 5. The transfer coefficient α is often taken equal to 0.5 in literature.[38–40]

$$b_f = \frac{RT}{\alpha \mathrm{F}}; \; b_b = \frac{RT}{(1-\alpha)\mathrm{F}} \qquad [5]$$

In Eq. 6 the expression for $\Delta\phi$ is given, where the Nernst correction for equilibrium potential has been already simplified since *SoC* equal to 50% is considered. It represents the potential difference computed between the solid electrode and liquid electrolyte at their interface, whose value is related to the overpotential η. Notice that, during discharge, η is defined positive for both V^{2+}/V^{3+} and VO^{2+}/VO_2^+ couple. Moreover, according to hypothesis (I), $\Delta\phi$ is not a variable of the spatial coordinate. Indeed, if the conductivity of

the electrolyte is sufficiently high, variations of ϕ_{el} can be neglected and this adds to the negligible decay of local Galvani potential in the solid metal.

$$\Delta\phi = \phi_s - \phi_{el} = E^0 + \eta \quad [6]$$

In the presented Butler Volmer Eqs. 3 and 4, two different kinetic rate constants are present for oxidation and reaction. However, these two parameters are not independent because they need to respect the open circuit condition (7).

$$k_b = k_f \exp\left(\frac{E^0 \mathrm{F}}{RT}\right) \quad [7]$$

When no crossover of vanadium ions occurs across the polymer membrane and side reactions are negligible (II), the total amount of vanadium ions within the electrode is constant. Considering the total concentration of vanadium ions homogeneous within the electrode (III) leads to considerable simplification. Indeed, introducing the state of charge SoC for the anolyte Eq. 8 and the catholyte Eq. 9, the Butler Volmer equation can be rewritten in the form Eq. 10, which applies to the two semi reactions and in which only one kinetic rate constant appears.

$$SoC = \frac{c_{V^{2+}}}{c_V} \quad [8]$$

$$SoC = \frac{c_{VO_2^+}}{c_V} \quad [9]$$

$$r = a\, k_f c_v\, SoC^s \left[\exp\left(\frac{\Delta\phi}{b_f}\right) + \exp\left(-\frac{\Delta\phi}{b_b} + \frac{E^0 \mathrm{F}}{RT}\right)\right] - a k_f c_v \exp\left(-\frac{\Delta\phi}{b_b} + \frac{E^0 F}{RT}\right) \quad [10]$$

Having introduced the above hypotheses allows to use one single form of the Butler Volmer for both negative and positive electrode. Furthermore, managing only two independent variables (SoC and $\Delta\phi$) considerably simplifies the problem.

Based on the above premises, the reaction rate in steady state is written in Eq. 10. The superscript 0 refers to steady state variables. The definition of the characteristic frequency of forward ω_f^* (11) and backward ω_b^* (12) reaction leads to a more compact expression of the reaction rate, which will be used in the following.

$$r_{BV}^0 = c_v[SoC_s^0(\omega_f^* + \omega_b^*) - \omega_b^*] \quad [10a]$$

$$\omega_f^* = a\ k_f \exp\left(\frac{\Delta\phi^0}{b_f}\right) \quad [11]$$

$$\omega_b^* = a\ k_b \exp\left(-\frac{\Delta\phi^0}{b_b} + \frac{E^0 F}{RT}\right) \quad [12]$$

Transport of reactants from pore center to active surface.—Inside the porous electrode, reactants transport from the center of the pores to active surface of carbon fibers where reaction takes place at a finite rate. This phenomenon is modelled as ions being transported across a boundary layer along the non-dimensional $\tilde{r}$ coordinate, which is normalized on the boundary layer thickness δ_{BL}. Such phenomenon accounts for the complex interaction of diffusive and convective mass transport and is described by the canonic steady state species transport equation with no source term accounting for electrochemical reactions, where electrophoretic migration term is neglected. The resulting equation is Eq. 13, where k is the global mass transport coefficient regulating the phenomenon, which accounts for both convective and diffusive mechanisms of transport to the surface, allowing to reduce the number of fitting parameters involved at pore scale mass transport. Boundary conditions for the problem consider the local state of charge at $\tilde{r} = 0$ equal to its value in the bulk of the electrolyte SoC_B^0 (14) and the presence of the electrochemical reaction at the carbon active surface, which advances at a local reaction rate r_{BV}^0 (15). The state of charge in the bulk of electrolyte SoC_B^0 is a function of the x-coordinate.

$$\frac{k}{\delta_{BL}^2}\frac{\partial^2 SoC^0}{\partial \tilde{r}^2} = 0 \quad [13]$$

$$\tilde{r} = 0 \rightarrow SoC^0 = SoC_B^0 \quad [14]$$

$$\tilde{r} = 1 \rightarrow \frac{k}{\delta_{BL}}\frac{\partial SoC^0}{\partial \tilde{r}} = -\frac{r_{BV}^0}{c_V\, a} \quad [15]$$

The resulting steady state distribution of SoC^0 across the boundary layer is written in Eq. 16. The rate of conversion of vanadium can be expressed in the form of Eq. 17 which is encountered in literature when modelling diffusive-convective mass transport at carbon fiber. In Eq. 17 the ratio $\frac{k}{\delta_{BL}}$ can be assimilated with mass transport coefficient found in literature, whose value is depending on geometrical features of electrode, rheological properties of electrolyte solutions and velocity field,[36,41] and it is later calibrated on experimental data.

$$SoC^0(\tilde{x}, \tilde{r}) = -\frac{\delta_{BL}\, r_{BV}^0}{c_V\, k\, a}\tilde{r} + SoC_B^0 \quad [16]$$

$$\frac{r_{BV}^0}{c_V\, a} = \frac{k}{\delta_{BL}}(SoC_B^0 - SoC_s^0) \quad [17]$$

The expression of r_{BV}^0 can be rewritten in terms of SoC_B^0 in the form of Eq. 18. Accounting for transport to electrode active surface has the effect of introducing the parameter ϵ^0 (19), which acts as a steady state effectiveness factor and tends to 1 for an infinite value of k, in the limit of negligible mass transport resistance to the electrode active surface.

$$r_{BV}^0 = c_v\ \epsilon^0[SoC_B^0(\omega_f^* + \omega_b^*) - \omega_b^*] \quad [18]$$

$$\epsilon^0 = \frac{\frac{ka}{\delta_{BL}}}{\omega_f^* + \omega_b^* + \frac{ka}{\delta_{BL}}} \quad [19]$$

Transport of reactants through electrode thickness.—Nernst–Planck equation regulates mass transport through the electrode. As stated in hypothesis (VI) migration is neglected. Moreover, in order to reduce the complexity and derive a fully analytical model, the contribution of advective transport is incorporated into the diffusion term. With this simplification transport in the bulk of electrolyte depends on a single transport parameter $\mathfrak{D}$ which is responsible for reactants distribution and depends on the velocity field. Hence, the steady state Nernst Planck equation simplifies to Eq. 20. According to (III), at the electrode/membrane interface no crossover is present, thus Eq. 21 is a valid boundary condition, while at the channel electrode interface a convective boundary condition is applied (22).

$$\frac{\mathfrak{D}}{\delta_{EL}^2}\frac{\partial^2 SoC_B^0}{\partial \tilde{x}^2} = a\frac{k}{\delta_{BL}}\frac{\partial SoC^0}{\partial \tilde{r}}\bigg|_{\tilde{r}=0} = \frac{r_{BV}^0}{c_V} \quad [20]$$

$$\tilde{x} = 0 \rightarrow \frac{\partial SoC_B^0}{\partial \tilde{x}} = 0 \quad [21]$$

$$\tilde{x} = 1 \rightarrow \frac{\partial SoC_B^0}{\partial \tilde{x}} = Pe[-SoC_{ch}^0 + SoC_B^0] \quad [22]$$

In Eq. 22 Pe represents the Peclet number, which is defined as:

$$Pe = \frac{h\delta_{EL}}{\mathfrak{D}} \quad [23]$$

The resulting transport equation for SoC_B^0 is given in Eq. 24. For very high values of Pe, the contribution due to concentration gradients at the channel/electrode interface disappears. The non-dimensional parameter λ_x^0 is defined according to Eq. 25: high values of λ_x^0 are typical of high current densities or sluggish diffusion and thus high overpotentials, and are responsible for a high consumption of SoC_B^0 along the x coordinate.

$$SoC_B^0(\tilde{x}) = \frac{SoC_{ch}^0 - \dfrac{\omega_b^*}{\omega_f^* + \omega_b^*}}{\cosh(\lambda_x^0) + \sinh(\lambda_x^0)\dfrac{\lambda_x^0}{Pe}}\cosh(\lambda_x^0\tilde{x}) + \frac{\omega_b^*}{\omega_f^* + \omega_b^*} \quad [24]$$

$$\lambda_x^0 = \delta_{EL}\sqrt{\frac{\epsilon^0(\omega_f^* + \omega_b^*)}{\mathfrak{D}}} \quad [25]$$

Proton charge balance and current density.—The proton current density along through electrode direction in steady state matches the reaction rate r_{BV}^0 and obeys to Eq. 26. The current density is solved considering an insulating electrode/channel interface (Eq. 27).

$$\begin{aligned}\frac{\partial j^0}{\partial \tilde{x}} &= -F\ \ \delta_{EL}\, r_{BV}^0 \ \ for\ \ positive\\ \frac{\partial j^0}{\partial \tilde{x}} &= F\ \ \delta_{EL}\, r_{BV}^0 \ \ for\ \ negative\end{aligned} \quad [26]$$

$$\tilde{x} = 1 \rightarrow j^0 = 0 \quad [27]$$

At the electrode/membrane interface ($\tilde{x} = 0$), the current density reaches its maximum and is indicated with j_{mem}^0, which is equal to the measured current density of the electrochemical cell. In Eq. 28 the ratio between $\tanh(\lambda_x^0)$ and λ_x^0 represents the zero-frequency limit of the Warburg-like impedance associated to the electrode, which will be defined during the development of the AC model.

$$j_{mem}^0 = F\delta_{EL}c_V\epsilon^0\left(\frac{SoC_{ch}^0 - \dfrac{\omega_b^*}{\omega_f^* + \omega_b^*}}{1 + \tanh(\lambda_x^0)\dfrac{\lambda_x^0}{Pe}}\frac{\tanh(\lambda_x^0)}{\lambda_x^0}\right)(\omega_f^* + \omega_b^*) \quad [28]$$

*Simulation of polarization curve.—*The potential difference of a symmetric cell is computed as Eq. 29 in which η_{red} and η_{oxi} are the overpotentials referred to cathode and anode, respectively. The reversible potentials are not present in the equation because they are equal for both reduction and oxidation.

$$\Delta V = \eta_{red} - \eta_{oxi} - \eta_{ohm} \quad [29]$$

η_{ohm} is the overpotential due to ohmic losses. It is mainly associated to the contribution of the polymeric membrane, which is assumed to give a purely ohmic response (VI). Other contributions to η_{ohm} include external circuit and bipolar plates. The conductivity of the separating membrane depends on parameters such as thickness, water content and concentration of the electrolyte. In this work, the membrane is simplified as a constant ohmic resistance (assumption VI).

$$\eta_{ohm} = j\ \ R_{mem} \quad [30]$$

When the transfer coefficient α of a redox couple is taken equal to 0.5 and SoC is equal to 50%, η_{red} and η_{oxi} are equal and opposite[37] and Eq. 29 can be rewritten into the form of Eq. 31.

$$\Delta V = 2\Delta\phi^0 - 2E^0 - j\ R_{mem} \quad [31]$$

The expression for j is implicit in the value of $\Delta\phi^0$ and the Matlab® routine *fsolve* is employed to simulate the polarization curve.

AC model development.—The development of the AC model follows a method based on Laplace transform: unsteady governing equations are written, nonlinear terms are linearized around the steady state and time dependent variables are decomposed into a steady state value X^0 and an oscillation with amplitude X^1 and angular frequency ω, so that $X = X^0 + X^1 e^{i\omega t}$. The steady equation is then subtracted and the differential equation for the transport of the AC variables in the frequency domain is obtained.[32]

The reaction rate r_{BV} is a function of SoC_s and $\Delta\phi$, which both oscillate around their steady state value with amplitudes SoC_s^1 and $\Delta\phi^1$ maintaining the same angular frequency ω of the imposed perturbation, as written in Eqs. 32 and 33. Being the applied perturbation small, the amplitude of reaction rate oscillation r_{BV}^1 can be linearized as in Eq. 34. Notice that in Eq. 34 SoC^1 and SoC^0 are the only variables dependent on spatial coordinates.

$$SoC_s = SoC_s^0 + SoC_s^1 e^{i\omega t} \quad [32]$$

$$\Delta\phi = \Delta\phi^0 + \Delta\phi^1 e^{i\omega t} \quad [33]$$

$$r_{BV}^1 = \frac{\partial r_{BV}^0}{\partial SoC_s^0}\bigg|_{\Delta\phi^0} SoC_s^1 + \frac{\partial r_{BV}^0}{\partial \Delta\phi^0}\bigg|_{SoC_s^0} \Delta\phi^1 \quad [34]$$

*Transport of reactants from pore center to active surface.—*According to the scheme depicted in Fig. 1, the model accounts for accumulation of vanadium ions and non-steady effects within the boundary layer at the active surface of electrode. Ion solvation and de-solvation processes as well as interaction with active sites on the active surface influence the electrode kinetics, whose fundamental mechanisms are still not fully understood.[42] A separate transport impedance, which is decoupled from the mass transport through the electrode thickness, is attributed to finite rate of mass transport at pore scale in the vicinity of active surface. Species balance equation along the r-coordinate is written accordingly in Eq. 35.

$$\frac{k}{\delta_{BL}^2}\frac{\partial^2 SoC}{\partial \tilde{r}^2} = \frac{\partial SoC}{\partial t} \quad [35]$$

After splitting AC and DC variables as previously described and subtracting the steady state equation, Eq. 35 is rewritten in the form of Eq. 36. Notice that, being SoC^1 the maximum amplitude of the perturbation, which is not variable over time, the derivative on the

right-hand side of the equation is conveniently written. Solution to Eq. 36 is subjected to boundary conditions in Eqs. 37 and 38, analogously to what discussed in 3.1.1.

$$\frac{k}{\delta_{BL}^2}\frac{\partial^2 SoC^1}{\partial \tilde{r}^2} = i\omega SoC^1 \quad [36]$$

$$\tilde{r} = 0 \rightarrow SoC^1 = SoC_B^1 \quad [37]$$

$$\tilde{r} = 1 \rightarrow \frac{\partial SoC^1}{\partial \tilde{r}} = -\frac{\delta_{BL}\, r_{BV}^1}{c_V\, k\, a} \quad [38]$$

The transport equation for SoC^1 is reported in Eq. 39 in which the parameter λ_r (40) has been introduced. For high values of λ_r, the perturbation propagates with higher intensity across the boundary layer and the phase shift induced by its dynamic behavior is enhanced. The role of λ_r can be explained in simple terms as an AC perturbation propagation factor: the higher its value, the stronger and faster the perturbation due to the boundary layer.

$$SoC^1(\tilde{x}, \tilde{r}) = SoC_B^1 \cosh(\lambda_r \tilde{r}) - \left[\frac{1}{\lambda_r \cosh(\lambda_r)}\frac{\delta_{BL}\, r_{BV}^1}{c_V\, k\, a} + SoC_B^1 \tanh(\lambda_r)\right]\sinh(\lambda_r\, \tilde{r}) \quad [39]$$

$$\lambda_r = \delta_{BL}\sqrt{\frac{i\omega}{k}} \quad [40]$$

In order to solve mass balance along the x direction it is convenient to express r_{BV}^1 in terms of SoC_B^0 and SoC_B^1. The full expression of r_{BV}^1 in reported in Eq. 41. With the same approach adopted for the DC case, ϵ_{SoC}^1 and $\epsilon_{\Delta\phi}^1$ are defined in (42) and (43), respectively: ϵ_{SoC}^1 and $\epsilon_{\Delta\phi}^1$ act as AC propagation factors and tend to 1 for an infinite value of. Moreover, ϵ_{SoC}^1 tends to ϵ^0 for values of ω approaching zero thus showing consistency with the DC model.

Transport of reactants through electrode thickness.—The Nernst Planck equation is written coherently with the DC case in the form (45), with the difference that in this case an accumulation factor is present. The geometric parameter χ is the ratio between the accumulation volume in which ions are solvated in the electrolyte and the total volume of the electrode. Notice that the remaining portion of electrode volume is occupied by carbon fibers and the boundary layer surrounding them, in which transport from the bulk of electrolyte to active surface occurs and is governed by Eq. 35.

$$\frac{\mathfrak{D}}{\delta_{EL}^2}\frac{\partial^2 SoC_B}{\partial \tilde{x}^2} = -\frac{\partial SoC}{\partial \tilde{r}}\bigg|_{\tilde{r}=0} a + \chi\frac{\partial SoC_B}{\partial t} \quad [45]$$

AC/DC decomposition leads to Eq. 46. Coherently with the DC case, at the electrode/membrane interface no ion crossover is present and boundary condition Eq. 47 is employed. At the channel/electrode interface, the solution is subjected to Eq. 48 where the amplitude of SoC perturbation in the bulk of the channel is null (assumption VII). The expression for $SoC_B^1(\tilde{x})$ is cumbersome and not reported here for sake of simplicity.

$$\frac{\mathfrak{D}}{\delta_{EL}^2}\frac{\partial^2 SoC_B^1}{\partial \tilde{x}^2} = -\frac{\partial SoC^1}{\partial \tilde{r}}\bigg|_{\tilde{r}=0} a + \chi i\omega\ SoC_B^1 \quad [46]$$

$$\tilde{x} = 0 \rightarrow \frac{\partial SoC_B^1}{\partial \tilde{x}} = 0 \quad [47]$$

$$\tilde{x} = 0 \rightarrow \frac{\partial SoC_B^1}{\partial \tilde{x}} = 0 \quad [48]$$

Proton current balance and impedance.—A non-Faradaic contribution due to the capacitive effect of the double layer appears in the AC proton current balance written in Eq. 49, where C_{DL} is the double layer capacitance.

$$\frac{\partial j}{\partial \tilde{x}} = -F\ \delta_{EL}\ r_{BV} - \delta_{EL} C_{DL}\frac{\partial \Delta\phi}{\partial t} \quad [49]$$

$$r_{BV}^1 = c_V\left\{\epsilon_{SoC}^1 SoC_B^1(\omega_f^* + \omega_b^*) + \epsilon_{\Delta\phi}^1 \epsilon^0 \Delta\phi^1\left[\left(SoC_B^0\epsilon^0 + \frac{\omega_b^*}{\omega_f^* + \omega_b^* + \frac{ka}{\delta_{BL}}}\right)\left(\frac{\omega_f^*}{b_f} - \frac{\omega_b^*}{b_b}\right) + \frac{\omega_b^*}{b_b}\right]\right\} \quad [41]$$

$$\epsilon_{SoC}^1 = \frac{\frac{\frac{ka}{\delta_{BL}}}{\cosh(\lambda_r)}}{\frac{ka}{\delta_{BL}} + (\omega_f^* + \omega_b^*)Z_{W_{BL}}} \quad [42]$$

$$\epsilon_{\Delta\phi}^1 = 1 - \frac{(\omega_f^* + \omega_b^*)Z_{W_{BL}}}{\frac{ka}{\delta_{BL}} + (\omega_f^* + \omega_b^*)Z_{W_{BL}}} \quad [43]$$

A Warburg-like element relative to the boundary layer surrounding carbon fibers Z_{WBL}, whose expression is given in (44).

$$Z_{W_{BL}} = \frac{\tanh(\lambda_r)}{\lambda_r} \quad [44]$$

The equation is written in terms of amplitudes of perturbation in the form Eq. 50 and solved considering null proton current at the channel/electrode interface Eq. 51. The amplitude of proton current perturbation at the electrode/membrane interface - indicated as j_{mem}^1 (52)—is equal to the measured current density perturbation.

$$\frac{\partial j^1}{\partial \tilde{x}} = -F\ \ \delta_{EL}\ \ r_{BV}^1 - i\omega\ \ \delta_{EL} C_{DL}\Delta\phi^1 \quad [50]$$

$$\tilde{x} = 0 \rightarrow j^1 = 0 \quad [51]$$

$$\tilde{x} = 0 \rightarrow j^1 = j_{mem}^1 \quad [52]$$

The impedance of the half-cell is calculated as in Eq. 53 and under the hypothesis of linearity it is independent from the value of applied

perturbation. The full expression for the impedance of the half-cell is given in Eq. 54. In the cumbersome expression of Z, terms relative to different transport phenomena appear bonded with each other. Thus, although developing an analytical model required consistent simplifications of governing equations, strong interplays between the included physical phenomena are present. Further analyses on the contributions of different transport phenomena on the total value of impedance will be presented in section 'Diagnosis of performance losses'.

$$Z = \frac{\Delta\phi^1}{j^1_{mem}} \qquad [53]$$

$$\frac{1}{Z} = \frac{j^0_{mem}}{\cosh(\lambda_r)} \times \frac{\epsilon^0 \epsilon^1_{SoC}\, \epsilon^1_{\Delta_\phi} \left(\frac{\omega^*_f}{b_f} - \frac{\omega^*_b}{b_b}\right)\left(1 - \frac{Z_w}{R_w} + \frac{Z_w}{Pe}(\lambda^{12}_x - \lambda^{02}_x)\right)\delta^2_{EL}}{\mathfrak{D}(\lambda^{02}_x - \lambda^{12}_x)\left(1 + \frac{\tanh(\lambda^1_x)\lambda^1_x}{Pe}\right)} + \frac{j^0_{mem}}{(\omega^*_o + \omega^*_r)}\left(\frac{\omega^*_f}{b_f} - \frac{\omega^*_b}{b_b}\right)\epsilon^0\epsilon^1_{\Delta_\phi} + i\omega C_{DL}\,\delta_{EL} + F\;\delta_{EL}\, c_V\, \epsilon^0 \left\{\left[\left(\frac{\omega^*_b}{\omega^*_f + \omega^*_b + \frac{ak}{\delta_{BL}}} + \frac{\epsilon^0\;\omega^*_b}{\omega^*_f + \omega^*_b}\right)\left(\frac{\omega^*_f}{b_f} - \frac{\omega^*_b}{b_b}\right) + \frac{\omega^*_b}{b_b}\right]\epsilon^1_{\Delta_\phi}\left[1 + \frac{\epsilon^1_{SoC}\;\lambda^{02}_x}{\epsilon^0\cosh(\lambda_r)\lambda^{12}_x} \times \left(\frac{Z_w}{1 + \frac{\tanh(\lambda^1_x)\lambda^1_x}{Pe}} - 1\right)\right]\right\} \qquad [54]$$

The parameter λ^1_x is defined in Eq. 55. For higher values of λ^1_x, the oscillation of state of charge propagates faster along the x direction. Such condition occurs in presence of high current density and sluggish kinetics and is typical of high values of overpotential. Under operation at high current density, SoC depletion through electrode thickness is more severe and stronger oscillations propagate. Moreover, in Eq. 55 the Warburg-like impedance relative to the electrode Z_w—whose expression is given in Eq. 56—appears. At values of ω approaching zero, λ^1_x tends to λ^0_x. In turn, Z_w tends to its limit R_w Eq. 57, which was encountered in Eq. 28 and shows coherence with the steady state derivation.

$$\lambda^1_x = \delta_{EL}\sqrt{\frac{1}{\mathfrak{D}}\left[\frac{\epsilon^1_{SoC}(\omega^*_f + \omega^*_b)}{\cosh(\lambda_r)} + \frac{\lambda_r \tanh(\lambda_r) ka}{\delta_{BL}} + i\omega\chi\right]} \qquad [55]$$

$$Z_w = \frac{\tanh(\lambda^1_x)}{\lambda^1_x} \qquad [56]$$

$$R_w = \frac{\tanh(\lambda^0_x)}{\lambda^0_x} \qquad [57]$$

Results and Discussion

Negative electrode.—The model is first validated against experimental data recorded on a negative symmetric cell. A procedure for calibrating unknown model parameters has been developed based on their impact on specific features of simulated impedance spectra. Further information related to this topic are included in the following and in Appendix A, where sensitivity analysis is also presented. Typical experimental EIS records from a negative electrode of a symmetric cell are reported in Fig. 2a, where it is clear that there are many features over the frequency range, which allow for independent or almost independent calibration of model parameters. The spectrum shows two distinct semicircles occurring at low and high frequencies, which are separated by a linear elongation of the second semicircle, here also called "linear branch." Relying on the sensitivity analysis reported in Appendix A, the fitting procedure decouples the effect of different parameters to fit features of the experimental spectra at different characteristic frequencies. It is hereby presented step by step:

1) The membrane resistance is calibrated on the high frequency resistance.
2) The double layer capacitance is calibrated on the Bode plot, specifically matching the imaginary impedance of the high frequency peak.
3) The kinetic rate constant k_f is calibrated on the radius of the high frequency semicircle of EIS.
4) The transport parameter $\mathfrak{D}$ is calibrated on the Bode plot, specifically matching the imaginary impedance of the low frequency peak.
5) The transport parameter k is calibrated on the linear branch.
6) The transport parameter h is calibrated on the value of low frequency resistance of EIS.

Model results at a flow rate of 20 ml min^{-1}.—The model is first tested against experiments at a flow rate equal to 20 ml min^{-1}. Operative parameters are summarized in the experimental section. Figure 2 depicts simulated and experimental EIS spectra taken at j = 0.1 A cm^{-2} and j = 0.05 A cm^{-2} at a flow rate of 20 ml min^{-1}.

In Fig. 2a, the experimental Nyquist plot is made up by two distinct features, which are typically referred as low frequency and high frequency loop of EIS. The first one resembles the shape of an ideal semicircle and is usually referred to charge transfer processes,[10,14] while the second one presents an elongated shape and looks like the superposition of two semicircles at overlapping frequencies, whose combination generates a linear branch. Such linear feature is present in other experimental data available in literature.[18] Phenomena generating the second loop of EIS typically encompass slow mass transport processes (i.e. involving heavy molecules or ions),[43] but there's lack of literature in the interpretation of such a feature for the specific case of VRFB technology. In Ref. 44 authors reported difficulties in modelling the linear branch. In Refs. 45, 46 this feature has been associated to a Warburg-like impedance and diffusive transport of ions through the electrode. However, such interpretation was not validated with experimental data. The model presented here is able to reproduce the linear branch observed in the experimental data.

Analyzing the two curves presented in Fig. 2a, the spectrum recorded at 0.1 A cm^{-2} shows more pronounced low frequency features and a higher value of zero frequency resistance, instead the high frequency feature is superimposed to the one measured at 0.05 A cm^{-2}. In Fig. 2b comparison between simulated and experimental spectra is shown. Assumed and fitted model parameters are summarized in Table I.

Particularly, fitted parameters are obtained applying the described procedure to the EIS spectrum recorded at 0.1 A cm^{-2}. The simulated curve at 0.05 A cm^{-2} is obtained maintaining the same set of parameters and repeating the simulation at the new value of current density. The fitted value of $\mathfrak{D}$ is in the same order of magnitude of the diffusivity reported Ref. 18, which was fitted using a through electrode 1D numerical model. Notice that the value of $\mathfrak{D}$

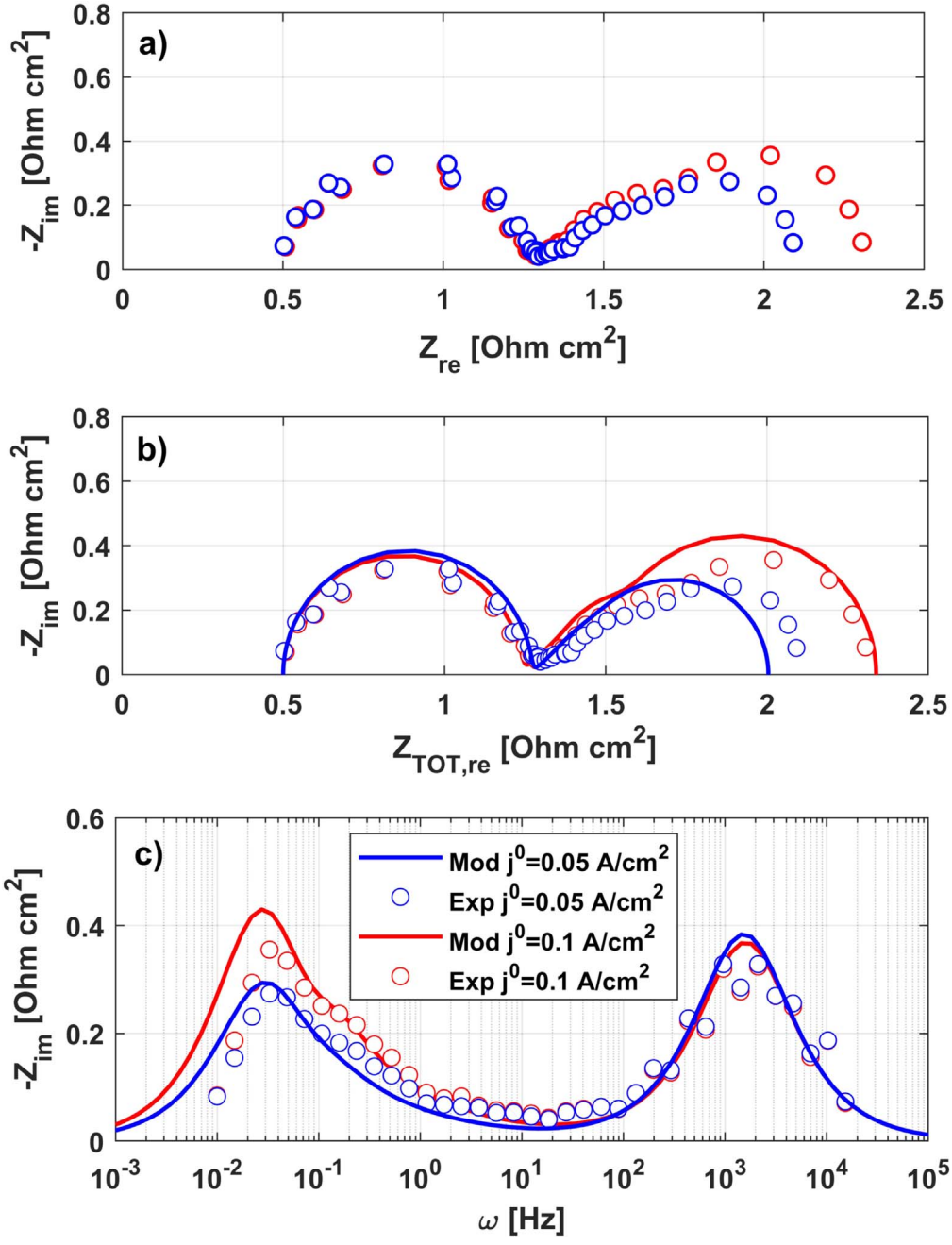

Figure 2. Comparison between experimental EIS (dots) and modelled spectra (continuous line) at $j = 0.1\ \mathrm{A\,cm^{-2}}$ (red) and $j = 0.05\ \mathrm{A\,cm^{-2}}$ (blue) at $20\ \mathrm{ml\ min^{-1}}$. Experimental Nyquist plot (a), simulated vs experimental Nyquist plot (b) and simulated vs experimental imaginary Bode plot (c).

reported in this work is higher: such a result was expected considering that the contribution of convection within the porous electrode was incorporated into $\mathfrak{D}$. Moreover, the developed model neglects the effect of depletion of vanadium ions along the channel and the propagation of oscillating concentrations. The mass transport coefficient k accounts for both convection and diffusion mechanisms at pore scale and therefore the resulting values strongly depend on the cell operating conditions, flow field geometry and electrode morphology. For this reason a comparison with the values reported in the literature is not trivial: in Ref. 49 higher values are reported, but the limiting current measurements used to extrapolate this parameter were performed with electrolyte characterized by different vanadium concentrations, different geometrical area of the cell, with parallel flow field and graphite felt electrodes.

Simulations and experiments show good qualitative and quantitative agreement regarding the main features and shape of the Nyquist plot as well as the measured and simulated relaxation frequencies in the Bode plot (Fig. 2c). The characteristic frequency of the first peak, mainly related to kinetics is around 10^3 Hz; the second peak of simulated EIS falls in the same frequency range of the experimental one (around 0.03 Hz). Furthermore, the model reproduces the trends of experimental data at a different current density with the same set of parameters. In particular, the radius of the second loop of EIS reduces and the linear branch that causes its elongation becomes less pronounced. In Fig. 2c the Bode plot related to the same curves show similar agreement.

Results of the DC simulation using the same set of parameters are depicted in Fig. 3. Modelled and simulated polarization curves at a flow rate equal to $20\ \mathrm{ml\ min^{-1}}$, which are displayed in Fig. 3a, show good agreement. The experimental polarization curve looks almost linear and makes difficult to identify different zones in which kinetics, activation losses or mass transport are dominant.[50] Such an

Table I. Assumed and fitted model parameters at 20 m min^{-1}.

Parameter	Value	Unit	
R_{mem}	0.5	Ω cm^2	Fitted
k_f	$1.4.10^{-2}$	cm s^{-1}	Fitted
a	$3.5.10^{2}$	cm^{-1}	47
α	0.5	—	48
C_{DL}	$1.2.10^{-2}$	F cm^{-3}	Fitted
k	$4.8.10^{-4.}\ \delta_{BL}$	cm^2 s^{-1}	Fitted
δ_{BL}	20	μm	Assumed
$\mathfrak{D}$	$5.0.10^{-5}$	cm^2 s^{-1}	Fitted
δ_{EL}	230	μm	measured
χ	0.2	—	Assumed
h	$3.5.10^{-2}$	cm s^{-1}	Fitted

observation gives further evidence on the need of EIS for the analysis of origin of internal losses. *SoC* profiles at 0.05 A cm^{-2} and 0.1 A cm^{-2} are shown in Figs. 3b–3d. As expected, a higher current density reflects in a more severe electrolyte consumption. Indeed, through electrode thickness (Fig. 3b), the red curve shows a significant drop of *SoC* related to the convection mechanism at the channel/electrode interface ($\tilde{x} = 0$). Additionally, a stronger decay occurs moving towards the membrane. Figures 3c and 3d depict the *SoC* profiles moving from the center of the pore ($\tilde{r} = 0$) to active surface ($\tilde{r} = 1$ at the channel/electrode interface and electrode/membrane interface, respectively. At a higher current density, the *SoC* profile looks steeper as more intense fluxes are necessary to sustain the reaction. Comparison between Figs. 3c and 3d shows that *SoC* gradients within the boundary layer in the pores are larger in the regions of the electrode near the channel, where local reaction rate peaks.

Model results at a flow rate of 10 ml min^{-1}.—The model is hereby validated against experimental data taken at a flow rate of 10 ml min^{-1}. Experimental and simulated spectra are depicted in Fig. 4. Comparison between Figs. 4a and 2a, shows a clear raise of the low frequency loop due to the onset of sluggish mass transport.

Fitting experimental curves at 10 ml min^{-1} requires recalibration of transport parameters. In Fig. 4a, a longer linear branch and an increased amplitude of the low frequency loop suggest a decrease of k and h, respectively. Moreover, physicochemical phenomena occurring in the cell, which contribute to the second loop, have higher characteristic time thus suggesting a decrease in $\mathfrak{D}$. Comparison between modelled and experimental Nyquist plot is shown in Fig. 4b. Mass transport coefficients are recalibrated on the EIS recorded at 0.1 A cm^{-2} and their new values are given in Table II. Comparison with previously fitted data is reported as well.

All the other model parameters are maintained equal to the ones in Table I. Lower values of transport parameters are coherent with the presence of lower velocities within the feeding channel and the electrode pores, and thus a poor distribution of reactants over its volume. The values of h is the most influenced by a change in flow

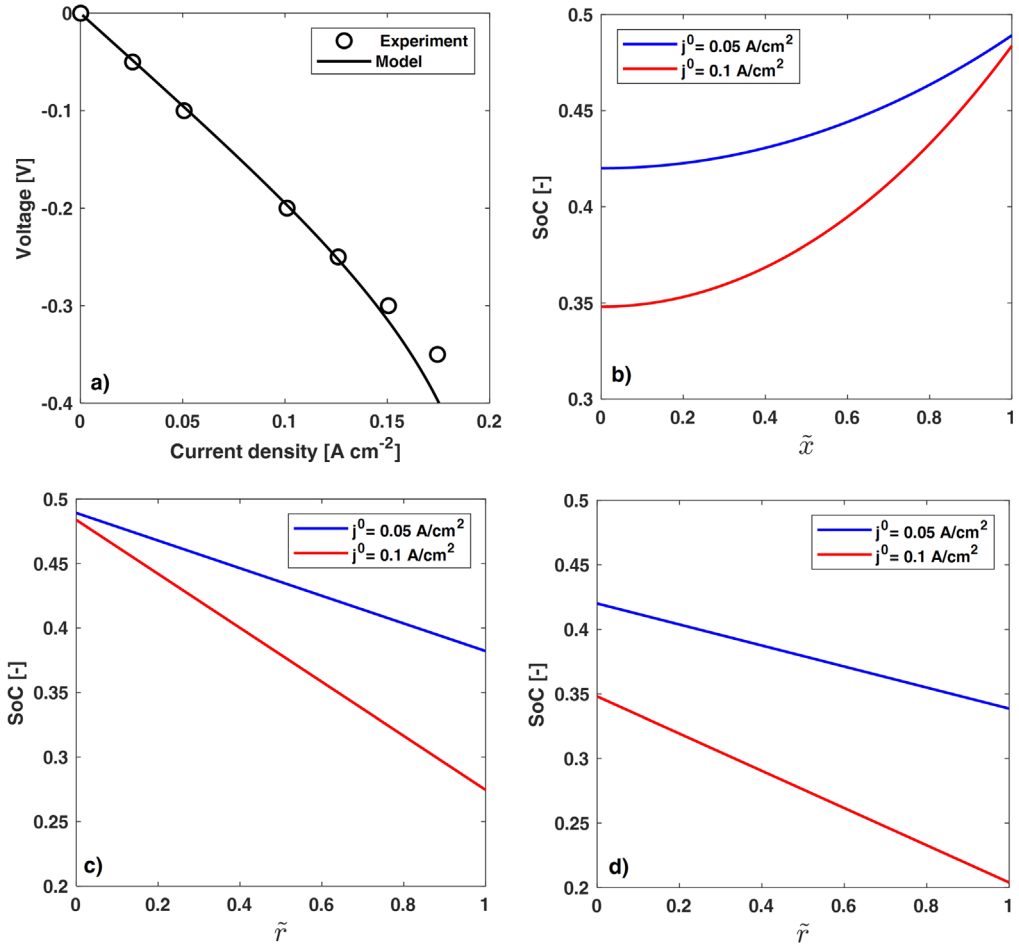

Figure 3. Results of DC simulation. Simulated (continuous line) vs experimental (dots) polarization curve taken at 20 ml min^{-1} (a), *SoC* profiles at j = 0.1 A cm^{-2} (red) and j = 0.05 A cm^{-2} (blue): $\tilde{x}$ direction from channel ($\tilde{x} = 1$) to membrane ($\tilde{x} = 0$) (b), within the boundary layer at electrode active surface ($\tilde{r} = 1$) for $\tilde{x} = 1$ (channel) (c) and $\tilde{x} = 0$ (membrane) (d). The non-dimensional $\tilde{x}$ coordinate is referred to δ_{EL}. The non-dimensional $\tilde{r}$ coordinate is referred to δ_{BL}.

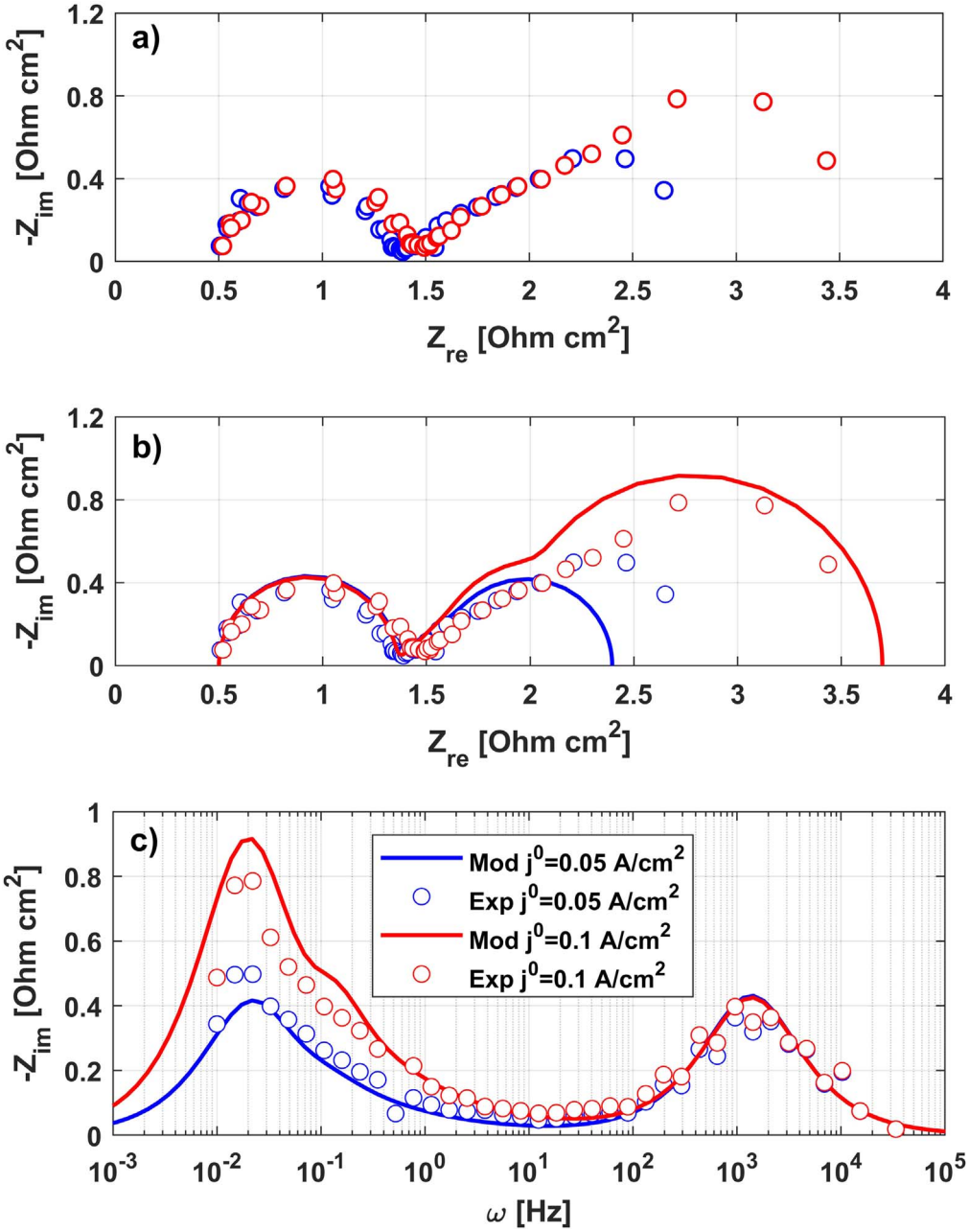

Figure 4. Comparison between experimental EIS (dots) and modelled spectra (continuous line) at $j = 0.1$ A cm^{-2} (red) and $j = 0.05$ A cm^{-2} (blue) taken at 10 ml min^{-1}. Experimental Nyquist plot (a), simulated vs experimental Nyquist plot (b) and simulated vs experimental imaginary Bode plot (c).

rate and reaches 40% of its initial value (−60% variation) in the passage from 20 ml min^{-1} to 10 ml min^{-1}. With the same change in flow rate, k decreases to 77% of its original value thus experiencing a −23% variation. These results are coherent with the observation that a change of flow rate causes a larger change of velocity in flow channel rather than in porous layer.[51] Moreover, lower velocities within the electrode determine a sluggish distribution of reactants, which reflects in a 16% decrease of $\mathfrak{D}$ (note that $\mathfrak{D}$ includes both diffusive and convective mechanisms). It has to be remarked that $\mathfrak{D}$ exhibits the lowest variation among the mass transport parameters, meaning that convection within the porous electrode is the least relevant among mass transport phenomena. As reported in Fig. 4b, moving to a value of current density equal to 0.05 A cm^{-2}, the simulation follows the decrease in length of linear branch and radius of the low frequency loop showed by experiments. Despite the model underestimates the total impedance at 0.05 A cm^{-2}, the main trends of impedance in the different conditions are followed, using a single set of parameters.

Figure 5 reports the experimental and simulated polarization curve at 10 ml min^{-1}. The decrease in performance at a lower flow rate reflects in higher values of overpotential with respect to Fig. 3a. In particular, the experimental polarization curve in Fig. 5, shows the beginning of a zone affected by mass transport limited conditions in which the slope of the polarization curve increases[50] (around 0.1 A cm^{-2}). Representations of

Table II. Values of recalibrated parameters employed in the simulation of at 10 ml min^{-1}. Values at 20 ml min^{-1} are reported for comparison.

Parameter	Value	Value at 20 ml min^{-1}	Unit
k	$3.7.10^{-4.}\ \delta_{BL}$	$4.8.10^{-4.}\ \delta_{BL}$	cm^2 s^{-1}
h	$1.4.10^{-2}$	$3.5.10^{-2}$	cm s^{-1}
$\mathfrak{D}$	$4.2.10^{-5}$	$5.0.10^{-5}$	cm^2 s^{-1}

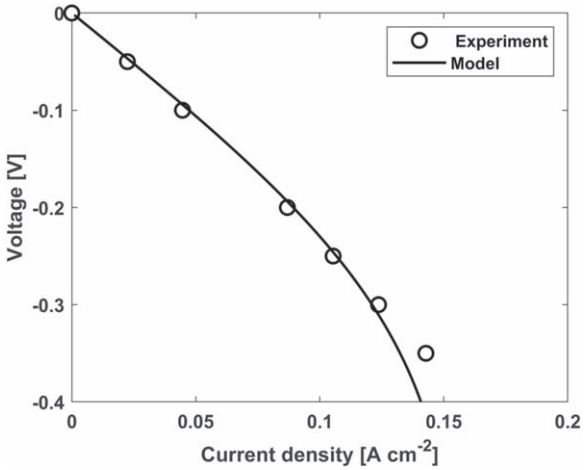

Figure 5. Simulated (continuous line) vs experimental (dots) polarization curve taken at 10 ml min^{-1}.

concentration profiles at 10 ml min^{-1} are steeper, but follow the trends reported in Figs. 3b–3d. Thus, they have been omitted for the sake of brevity. The lowest value of SoC within the electrode—which occurs at the electrode active surface for $\tilde{x} = 0$ (membrane)—is in this case equal to 18%, less than half the corresponding value at 20 ml min^{-1} (38%).

The model showed good capability to fit experimental spectra recorded on negative symmetric cell at different values of current density and flow rate. In the following, the model will be used to interpret data on a positive symmetric cell.

Positive electrode.—The model is hereby validated against experimental data recorded on a positive symmetric cell. The interpretation of EIS spectra for VRFB positive electrode is further complicated by the absence of two distinct semicircles in the Nyquist plot. It has been observed that the V^{2+}/V^{3+} couple of negative electrode is affected by a sluggish kinetics with respect to the VO^{2+}/VO_2^{+} at the positive electrode[52] and this leads to a higher kinetic resistance and a separation of the kinetic loop from the one related to mass transport. Due to the absence of a distinct and evident high frequency semicircle the value of double layer capacitance is not relevant and thus its value is not fitted. The absence of a first distinct semicircle requires to adopt an alternative strategy to fit the kinetic constant with respect to the one used before. To calibrate k_f we use the point of the polarization curve at the lowest current density, where activation losses dominate and mass transport limitations are not present—a procedure already used in.[53]

Model results at a flow rate of 20 ml min^{-1}.—Figure 6a shows two distinct experimental spectra recorded on a positive symmetric cell at a flow rate of 20 ml min^{-1} and current densities equal to 0.2 A cm^{-2} and 0.05 A cm^{-2}.

A comparison with Fig. 2 evidences lower values of impedance recorded on the positive electrode and the absence of a high frequency distinct semicircle. Each one of the two curves exhibit a long linear branch, that resembles in shape the feature seen in Figs. 2a and 4a. The comparison between the two curves shows that an increased current density reflects in a longer linear branch and a larger low frequency feature.

In figure 6b simulated Nyquist plot are plotted over experiments. Model parameters employed in the simulation are summarized in Table III.

Fitted parameters are calibrated using the experimental EIS recorded at 0.2 A cm^{-2}. Subsequently, the simulation is repeated maintaining the same set of parameters, but at a current density of 0.05 A cm^{-2} to obtain the second simulated spectrum. The values of parameters are in the same order of magnitude to those found for the

Table III. Assumed and fitted model parameters at 20 m min^{-1}.

Parameter	Value	Unit	
R_{mem}	0.38	Ω cm^2	Fitted
k_f	$1.0.10^6$	cm s^{-1}	Fitted
a	$3.5.10^2$	cm^{-1}	47
α	0.5	—	48
k	$1.8.10^{-3.}\ \delta_{BL}$	$cm^2\ s^{-1}$	Fitted
δ_{BL}	20	μm	Assumed
$\mathfrak{D}$	$6.0.10^{-5}$	$cm^2\ s^{-1}$	Fitted
δ_{EL}	230	μm	measured
χ	0.2	—	Assumed
h	9.10^{-2}	cm s^{-1}	Fitted

negative symmetric cell, except for the case of a higher kinetic rate constant, which is found for the positive electrode in accordance with the lower kinetic resistance typical of the positive electrode. This result is in line with Ref. 52. The fitted value of k_f is high enough to imply EIS in which the high frequency feature is not appreciable and a simulated polarization curve which shows good agreement with the experimental data at values close to OCV[53] (Fig. 7). Simulations and experiments show good agreement and the phenomena included in the model well describe the main features of EIS. When changing operating current, the model correctly reproduces the trend shown by experiments with satisfactory accuracy. Figure 6c depicts the imaginary Bode plot on which the value of $\mathfrak{D}$ has been fitted: the characteristic frequency of the peak is the same for the two values of j and falls around 0.08–0.09 Hz.

The experimental polarization curve recorded on the same cell is presented in Fig. 7. The positive symmetric cell shows a higher operating current density compared to the negative symmetric cell (see Fig. 3) and this evidence is coherent with the lower value of impedance recorded for the positive cell and the strongly limited kinetic regime typical of the negative electrode. The simulation is a good fit to experimental data and reproduces their features, exhibiting strong mass transport limitations from around 0.3 A cm^{-2} on.

Model results at a flow rate of 10 ml min^{-1}.—Similarly to the results reported for the negative electrode, a decrease in flow rate enhances mass transport limitations, in which it caused an increased radius of first and second semicircle of EIS. In Fig. 8a, two experimental EIS recorded at a current density of 0.2 A cm^{-2} and 0.05 A cm^{-2} and at a flow rate of 10 ml min^{-1} are displayed. The features of the spectrum are the same of those observed in Fig. 6a, in which the effect of mass transport limitation becomes more evident with the decrease in flow rate. Indeed, in the passage from 20 ml min^{-1} to 10 ml min^{-1}, the linear branch becomes longer and the total impedance of the symmetric cell increases. Moreover, the peak in Fig. 8c shifts towards lower frequencies with respect to Fig. 6c meaning that mass transport has a lower characteristic frequency.

The observed trends guide the refitting of transport parameters, whose value are reported in Table IV.

The parameter k experiences a 28% decrease, associated to lower velocities within the electrode and indicating sluggish mass transport to carbon active surface. At the electrode/channel interface, lower velocities within the feeding channel are highlighted by a 72% decrease of h. Distribution of reactants through the electrode shows a reduction of the transport parameter $\mathfrak{D}$ of about 8%: it is worth remarking that $\mathfrak{D}$ is experiencing the lowest decrease among the recalibrated parameters, as previously discussed in section 'Model results at a flow rate of 10 ml min^{-1}' for the negative symmetric cell. In Fig. 8b, the simulations and experiments are compared after recalibration of parameters with the experimental curve recorded at 0.2 A cm^{-2}. Good agreement is shown both in terms of EIS features and trend at changing current density.

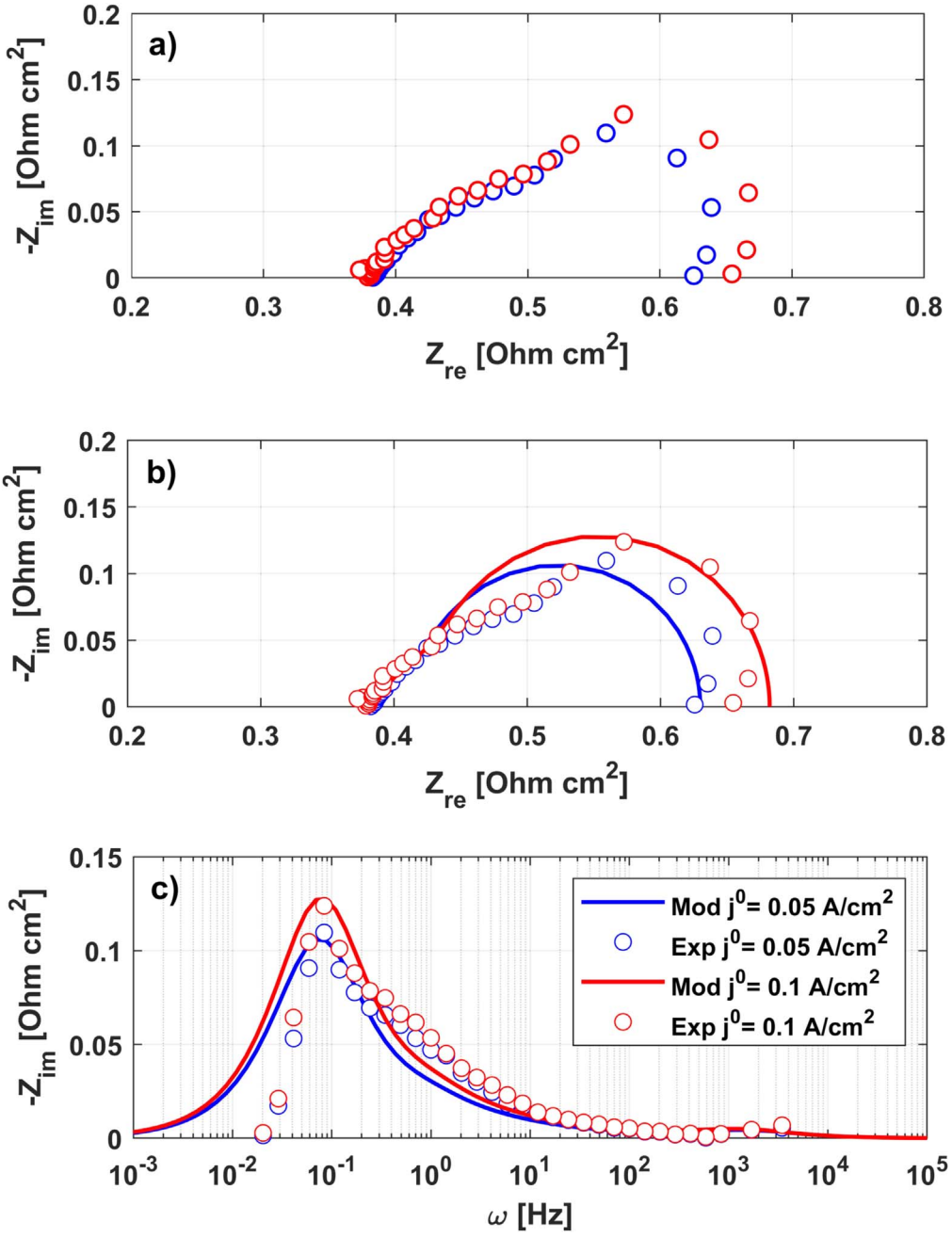

Figure 6. Comparison between experimental EIS (dots) and modelled spectra (continuous line) at $j = 0.2$ A cm^{-2} (red) and $j = 0.05$ A cm^{-2} (blue) taken at 20 ml min^{-1}. Experimental Nyquist plot (a), simulated vs experimental Nyquist plot (b) and simulated vs experimental imaginary Bode plot (c).

The decrease in performance at a lower flow rate is reflected in the experimental polarization curve depicted in Fig. 9 where a decrease in limiting current is seen with respect to Fig. 7:as a matter of facts, the mass transport limited region shifts to lower values of current density and overpotentials increase. From the comparison with the DC model, a good agreement is maintained also at lower flow rate.

The impedance model developed has been proved to be a suitable tool to interpret EIS spectra recorded also on a positive symmetric cell. Indeed, it has been shown to be successful in following trends at different current densities and flow rates with an approach based on physics.

Diagnosis of performance losses.—The analytical expression for the impedance of a VRFB electrode has been derived and reported in Eq. 54, but an interpretation of the contribution of different transport phenomena is difficult to perform due to strong interplays between them. With the aim of further analyzing the different causes of loss and their relative contribution, limits of AC and DC solutions were derived, with the aim of simultaneously eliminating the contribution of specific mechanisms in the expression of impedance and steady

Table IV. Values of recalibrated parameters employed in the simulation at 10 ml min^{-1}. Values at 20 ml min^{-1} are reported for comparison.

Parameter	Value	Value at 20 ml min^{-1}	Unit
k	$1.3.10^{-3}.\ \delta_{BL}$	$1.8.10^{-3}.\ \delta_{BL}$	cm^2 s^{-1}
h	$2.5.10^{-2}$	9.10^{-2}	cm s^{-1}
$\mathfrak{D}$	$5.5.10^{-5}$	$6.0.10^{-5}$	cm^2 s^{-1}

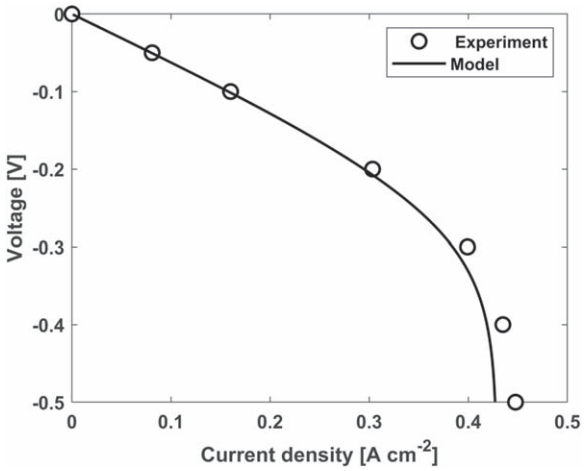

Figure 7. Simulated (continuous line) vs experimental (dots) polarization curve taken at 20 ml min^{-1}.

state current density. The limits for infinite value of mass transport coefficients k, h, $\mathfrak{D}$ and null C_{DL} are calculated, as shown in (Eqs. 58–61), where Z_{ct} represents the contribution of charge transfer, Z_k is associated to the transport of reactants from pore center to active surface, while Z_h and $Z_{\mathfrak{D}}$ are related to the transport of reactants in the channel and through the electrode, respectively. The reader can refer to Fig. 1 for a schematic of the model and impedances. The analytical expressions, not reported for the sake of brevity, have been implemented into the model obtaining thus the values of the impedance related to the single physical phenomenon in each simulated condition.

$$Z_{ct} = \lim_{\substack{k\to+\infty \\ h\to+\infty \\ \mathfrak{D}\to+\infty}} Z \quad [58]$$

$$Z_k = \lim_{\substack{C_{DL}=0 \\ h\to+\infty \\ \mathfrak{D}\to+\infty}} Z \quad [59]$$

$$Z_h = \lim_{\substack{k\to+\infty \\ C_{DL}=0 \\ \mathfrak{D}\to+\infty}} Z \quad [60]$$

$$Z_{\mathfrak{D}} = \lim_{\substack{k\to+\infty \\ h\to+\infty \\ C_{DL}=0}} Z \quad [61]$$

Diagnosis of losses at negative elctrode.—The impedance of negative symmetric cell has been decomposed according to the procedure described in section 'Diagnosis of performance losses'. Each electrode is represented with four impedances related to single physical phenomena (Eqs. 58–61), whose analytical expressions have been obtained. Finally, the separating membrane is modelled as an additional electric resistance. Such an approach is useful in the diagnosis of different causes of loss. Specifically, being each impedance directly related to a single transport phenomenon, evaluating its contribution gives a direct indication of how much the related physicochemical process contributes to the total loss of power density.

The diagnosis of the different causes of loss for the negative electrode in all the investigated operating conditions is reported in Fig. 10. For each tested condition a bar chart and a Bode plot are reported. The bar chart shows how the total value of overpotential is distributed on the different equivalent circuital elements Z_{ct} (blue), $Z_{\mathfrak{D}}$ (red), Z_h (yellow), Z_k (green) derived from the asymptotical analysis. Each bar shows a zero-frequency limit and corresponds to the value of one of the corresponding resistances R_{ct}, $R_{\mathfrak{D}}$, R_h, R_k. Results are normalized on the total cumulative resistance (sum of R_{ct}, $R_{\mathfrak{D}}$, R_h, R_k) in order to show the relative weight of each transport loss. The ionic resistance attributed to the membrane and electric resistances of electrodes and current collectors are not included in the presented results because the values fitted in the previous sections already give a quantitative evaluation of the impact on performance loss. Beside each bar chart, a Bode plot corresponding to the same operative conditions is present. The Bode plot gives complementary information on the frequency ranges at which each of the four computed impedances affects the spectra. For each single value of ω, it shows the share of total simulated impedance among the four computed elements. It is worth noting that mass transport phenomena affect VRFB impedance also at high frequency, in particular at high current and low flow rate. This behavior further highlights the complexity in the interpretation of experimental measurements and the usefulness of the developed model. Thus, the bar chart and Bode plots together are able to give interesting insights on the single causes of performance losses and how each physicochemical phenomenon shapes the EIS spectrum.

Figure 10a refers to a current density of 0.05 A cm^{-2} and a flow rate of 20 ml min^{-1}. Charge transfer processes are the main contributors to the total loss as they account for 44% of the total half-cell resistance. The charge transfer impedance relates to processes with high characteristic frequencies and contributes to the first feature of EIS, while it does not affect the second semicircle. The biggest part of the low frequency element of EIS is due to transport of ions from the center of the pores to pore active surface Z_k. Its contribution is 34% of the total resistance. Another meaningful contribution comes from transport of ions through the electrode coordinate (17% of total resistance). Convection at the channel/electrode interface does not have a strong impact on performance in this operating condition (4% in the bar chart). In Fig. 10b the analysis is performed at a current density of 0.1 A cm^{-2} and a flow rate of 20 ml min^{-1}. Comparison with Fig. 10a shows that an increased current causes the charge transfer impedance to account for a lower share of the total loss (20% for the half cell) and a greater relative contribution of Z_k, Z_h and $Z_{\mathfrak{D}}$ in determining the amplitude of the high frequency feature. The decrease of R_{ct} splits among the impedances related to other transport phenomena, which increase in relative terms and cause the second semicircle to prevail on the first one. The biggest increase is seen in R_k, which accounts for 55% of total resistance. Contributions related to $R_{\mathfrak{D}}$and R_h account for 20% and 5%, respectively. Figure 10c refers to a current density of 0.05 A cm^{-2} and a flow rate of 10 ml min^{-1}. It has been observed that an increase in flow rate causes mass transport coefficients to decrease and values of re-calibrated transport coefficient are reported in Table II. The charge transfer impedance is not affected by a change in flow rate, however, its relative contribution to the total loss decreases (32% in the bar chart) because losses related to other transport phenomena become more relevant. Particularly, R_h increases and its contribution reaches 11% of the total half-cell resistance. Also, R_k accounts for the largest share of losses as its contribution reaches 40%. Transport of vanadium ions through the electrode coordinate becomes sluggish due the decrease in $\mathfrak{D}$ with flow rate and its relative contribution to the total half-cell resistance equals 17%. Figure 10d refers to a current density of 0.1 A cm^{-2} and a flow rate of 10 ml min^{-1}. In this case R_{ct} accounts for only 5% of the total half-cell resistance and only a small part of the first semicircle of EIS is due to Z_{ct}. The low frequency peak of EIS predominates and reaches three times the value of the high frequency peak. Among all contributions, R_k dominates and accounts for 72% of the total half-cell resistance. The contribution of $R_{\mathfrak{D}}$ in the bar chart exhibits a different trend at increasing current density for different values of flow rate. Indeed, it decreases from 17% to 12% when j increases from 0.05 A cm^{-2} to 0.10 A cm^{-2} at a flow rate equal to 10 ml min^{-1}. On the other side, it increases from 17% to

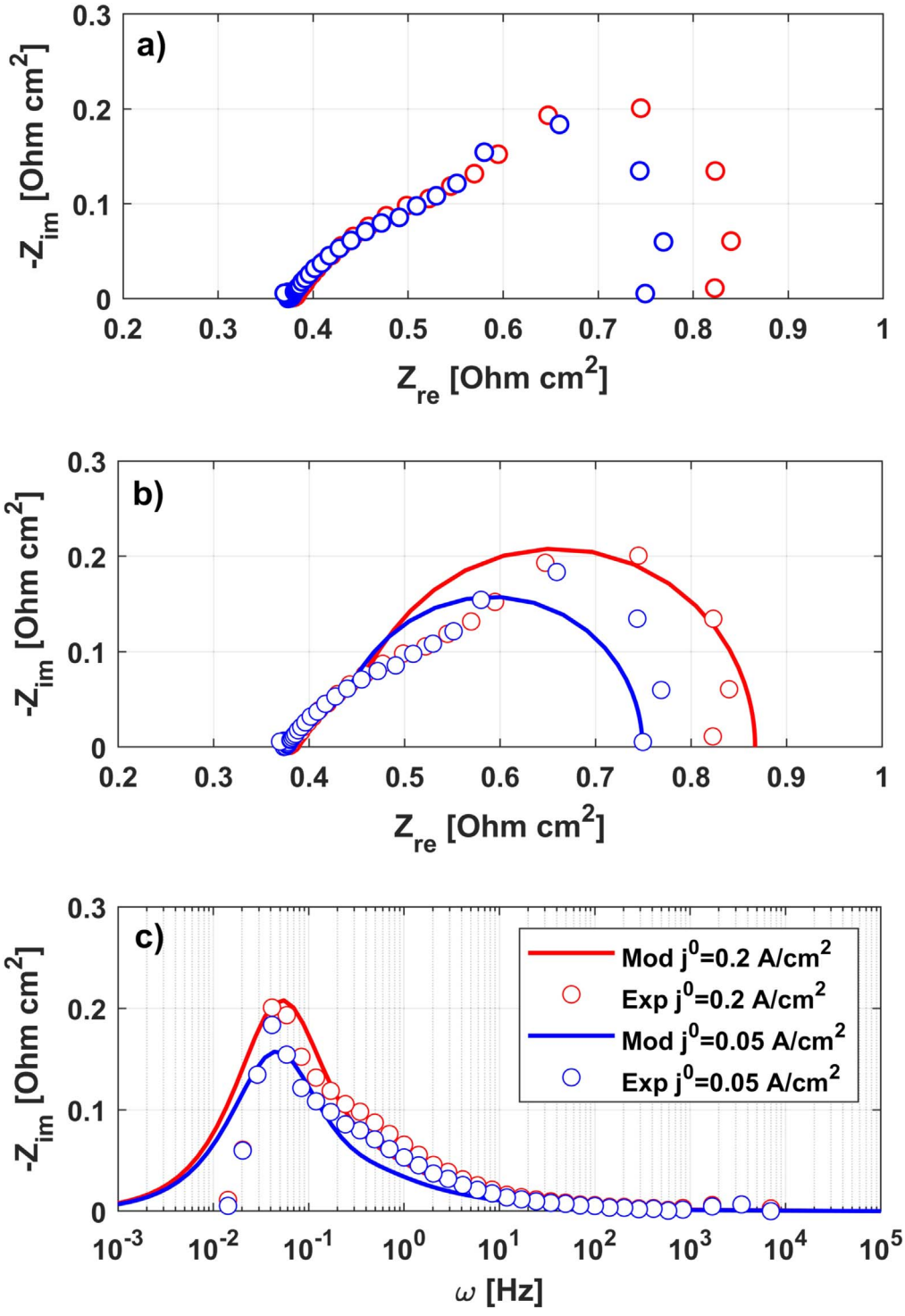

Figure 8. Comparison between experimental EIS (dots) and modelled spectra (continuous line) at $j = 0.2$ A cm^{-2} (red) and $j = 0.05$ A cm^{-2} (blue) taken at 10 ml min^{-1}. Experimental Nyquist plot (a), simulated vs experimental Nyquist plot (b) and simulated vs experimental imaginary Bode plot (c).

20% with the same change in j at a flow rate equal to 20 ml min^{-1}. It can be concluded that at lower values of flow rates, transport of ions to the active surface of the electrode is the limiting phenomenon. On the other side, at higher flow rates, the increased values of transport parameters k and h cause the corresponding losses to become less important and reactants distribution along the through electrode coordinate to become critical.

Diagnosis of losses at positive electrode.—Diagnosis of different causes of loss is repeated for the positive symmetric cell: the results of the analysis are shown in Fig. 11. Figure 11a refers to a current density of 0.05 A cm^{-2} and a flow rate of 20 ml min^{-1}. The charge transfer impedance does not cause a considerable loss in the case of a positive electrode in accordance with the absence of a distinct high frequency semicircle. The impedance due to mass transport from center of pores to active surface of carbon is the main responsible for performance loss: its contribution to the total resistance is equal to 80%. Transport of vanadium ions along the through electrode direction is the second cause of loss and accounts for 13% of the total half-cell resistance. In Fig. 11b the analysis is repeated with the

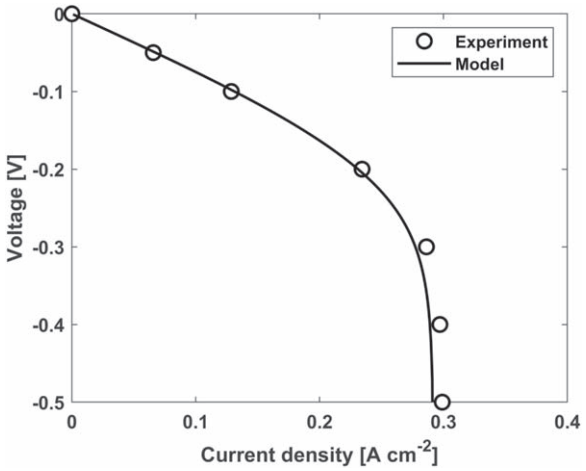

Figure 9. Simulated (continuous line) vs experimental (dots) polarization curve taken at 10 ml min^{-1}.

same set of parameters and a current density equal to 0.2 A cm^{-2}. Comparison with Fig. 11a shows a higher value of total impedance. However, the ranking order of contributions to the total performance loss does not vary between the two cases and it is in descending order R_k, $R_{\mathfrak{D}}$, R_h, R_{ct} (not considering R_{ohm}). Values of transport coefficients fitted at a flow rate equal to 10 ml min^{-1} are given in Table IV. At a flow rate of 10 ml min^{-1}, R_h becomes the second contributor to the total resistance of the half-cell (see Figs. 11c and 11d): in the bar chart related to a current density of 0.05 A cm^{-2} R_h is equal to 15% (Fig. 11c), which is more than two times its value at the same current density and a flow rate of 20 ml min^{-1} (6% in Fig. 11a). Thus, we observe that, at low values of flow rate, convection in the channel becomes relevant in terms of performance loss. This behavior could be addressed to a greater sensitivity of the convection between channel and electrode to the value of flow rate, and thus of velocity, for the positive electrode, while the mass transport through the porous medium is less dependent on velocity, and so limited by diffusion. It is also worth noting that, passing from 20 ml min^{-1} to 10 ml min^{-1}, the relative contribution of R_k is reduced and in the calibration process part of this reduction could have been compensated by a raise of R_h. This happens in a limited amount of cases, but a further analysis will be carried out in the future to better distinguish the different contributions. Moreover, it is known in the literature that the positive electrode is more affected by mass transport phenomena, so a relevant effect of fluid dynamics, not modelled in the presented work, could have been included in the calibration of the h parameter. Finally, it is possible to conclude that, for the case of the positive electrode, Z_k is the main responsible for the performance loss and dominates over the others.

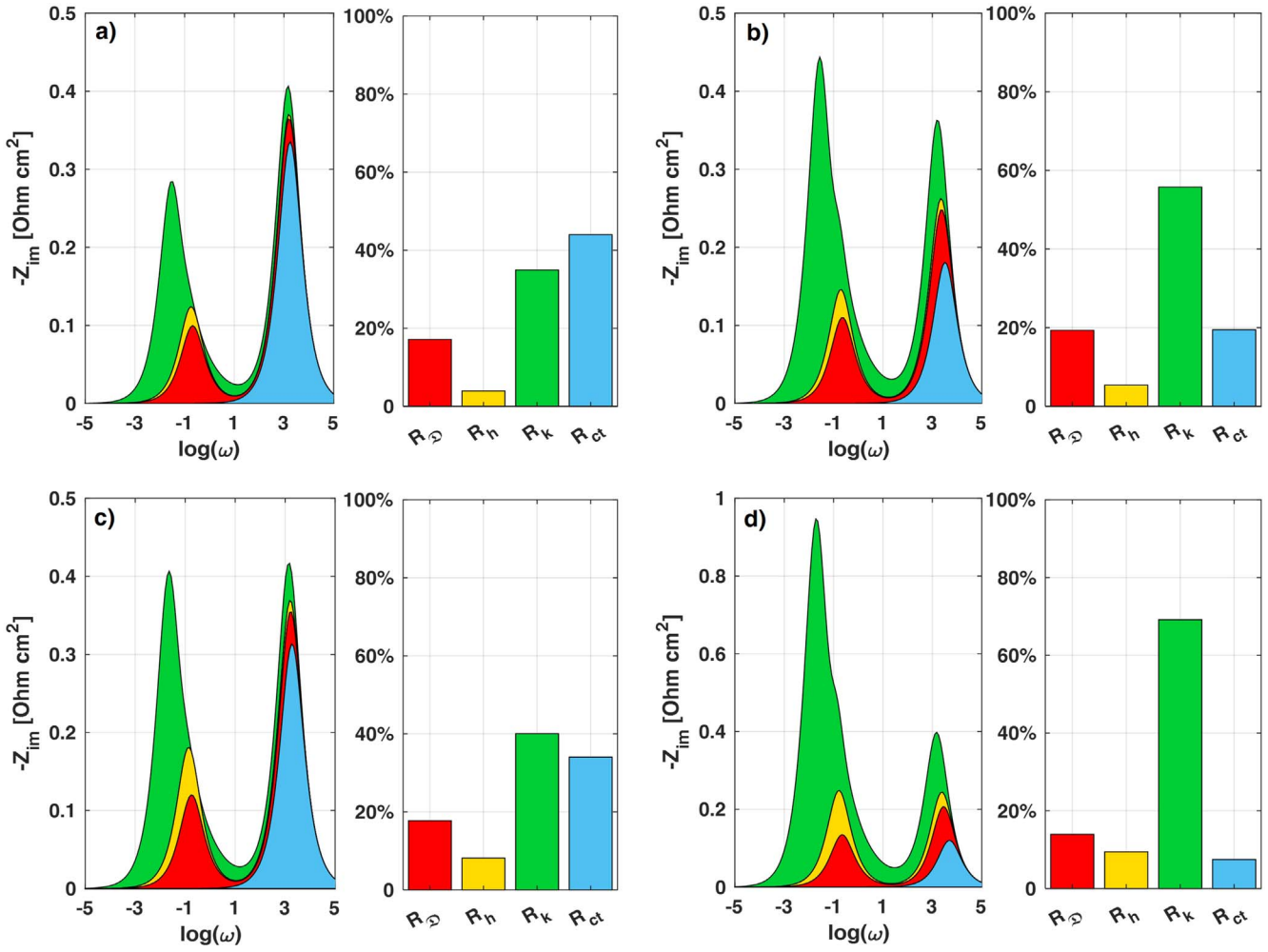

Figure 10. Impedance spectra and resistances associated to different physical phenomena for the case of a negative symmetric cell. Operative conditions: 0.05 A cm^{-2} 20 ml min^{-1} (a), 0.1 A cm^{-2} 20 ml min^{-1} (b), 0.05 A cm^{-2} 10 ml min^{-1} (c), 0.1 A cm^{-2} 10 ml min^{-1} (d).

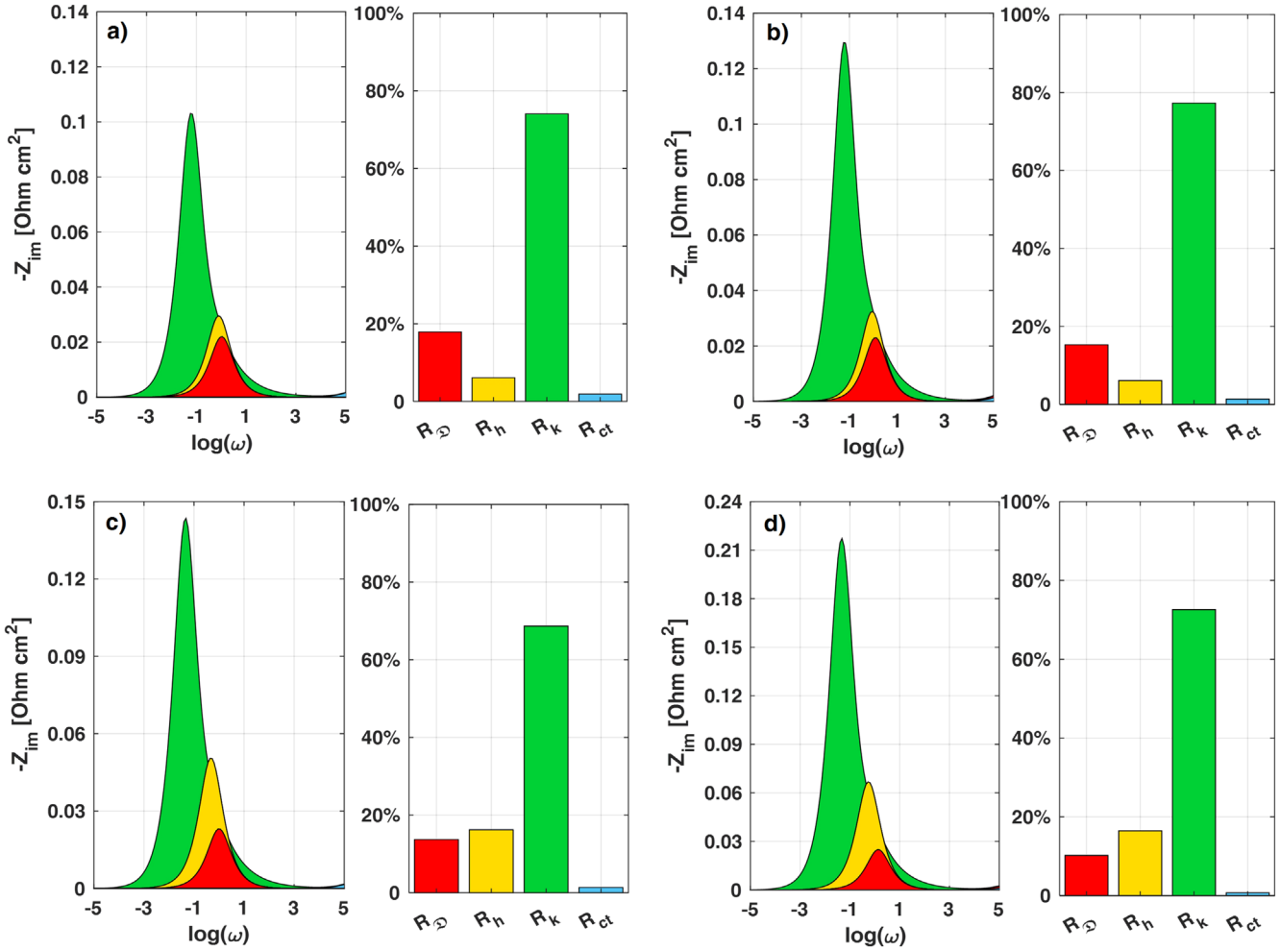

Figure 11. Impedance spectra and resistances associated to different physical phenomena for the case of a positive symmetric cell. Operative conditions: 0.05 A cm^{-2} 20 ml min^{-1} (a), 0.2 A cm^{-2} 20 ml min^{-1} (b), 0.05 A cm^{-2} 10 ml min^{-1} (c), 0.2 A cm^{-2} 10 ml min^{-1} (d).

Conclusions

A 1D fully analytical model for the impedance of a VRFB electrode is developed. The model includes losses associated with charge transfer kinetics, vanadium ion diffusion and advection through the electrode thickness, convection between the flow channel and the porous electrode (Sigracet® SGL 39 AA carbon paper) and mass transport in the boundary layer surrounding the carbon fiber (active surface of the electrode). Comparison with experimental data recorded using symmetric cell architecture shows good results for both positive and negative electrode at two values of current density and flow rate. The model represents a suitable tool for the consistent interpretation of EIS spectra at different operative conditions. Moreover, being the model fully analytical, it allows for fast processing of experimental spectra and can be adapted to be employed into high-throughput studies. In order to accelerate improvement of flow battery technology the model is made available online at http://mrtfuelcell.polimi.it. Experimental results exhibit a linear feature in the frequency range 10 Hz to 0.1 Hz, which has been attributed to transport from the center of the pore to the active surface of electrode. Subsequently, by means of asymptotical analysis each single physical phenomenon included in model is associated to a specific impedance, highlighting its contribution in the investigated operative conditions. It is found that—for the negative electrode - transport of vanadium ions to the active surface of the electrode is the limiting phenomenon at lower flow rates. On the other side, at higher flow rates, the increased values of transport parameters k and h cause the corresponding losses to become less important and reactants distribution along the through electrode coordinate to become critical together with charge transfer processes, whose influence in more relevant al low current densities. For the positive electrode, Z_k is the main responsible for the performance loss and dominates over the others. Considering that the fluid dynamics is not modelled, further studies in which analytical modelling is coupled with CFD may help to further understand and decompose its contribution. The presented model does not account for additional effect of depletion of vanadium ions along the channel direction in consequence of insufficient or limited reactant feeding. In future work the authors plan to extend the model to achieve a complete analytical description of ion distribution in a symmetric flow battery single cell, providing insights into local impedance behavior.

Appendix A. Sensitivity Analysis

Sensitivity analysis is hereby performed for the negative symmetric cell to show how variations of fitted parameters affect impedance simulations. The following results have supported the fitting procedure used in this manuscript. Operative and model parameters used in the reference case are given in the experimental section and Table I, respectively. Moreover, each investigated parameter is in turn increased (+50%) or decreased (−50%) while all others are kept constant. Curves are modeled at j = 0.1 A cm^{-2}.

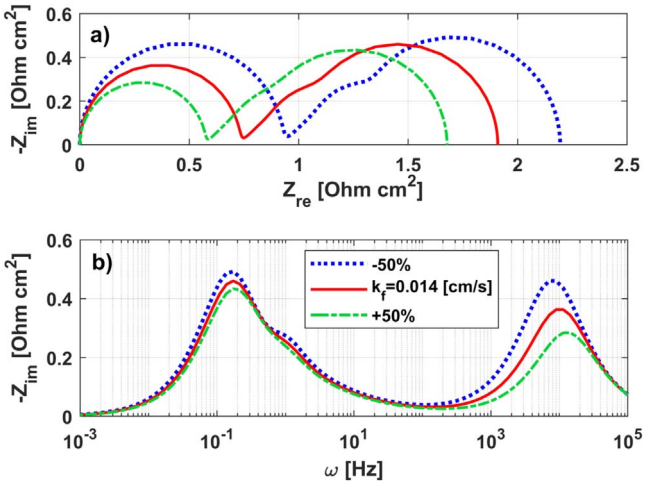

Figure 12. Influence of kinetic rate constant on Nyquist plot (a) and Bode plot (b).

A.1. Kinetic rate constant.—Figure 12 shows the effect of a variation in k_f on the simulated spectra.

A lower kinetic constant reflects in an increased impedance. Most of the increase is due to greater radius of the high frequency loop, which is directly related with kinetics (see Fig. 12a). Moreover, the low frequency loop is not sensitive to a variation of k_f. In Fig. 12b it is seen that both characteristic frequencies of the two loops decrease as kinetics become more sluggish.

A.2. Double layer capacitance.—A change in C_{DL} reflects on a shift of the high frequency peak of EIS. In particular, an increase in C_{DL} causes the peak to move towards lower frequencies - a result already presented and discussed for the case of a HT-PEMFC in.[53] However, as the low and high frequency peaks are far and don't overlap, a change of C_{DL} in the considered range has no effect on the simulated Nyquist plot.

A.3. Transport coefficient D.—$\mathfrak{D}$ is responsible for transport of reactants through electrode thickness. A decrease in $\mathfrak{D}$ causes

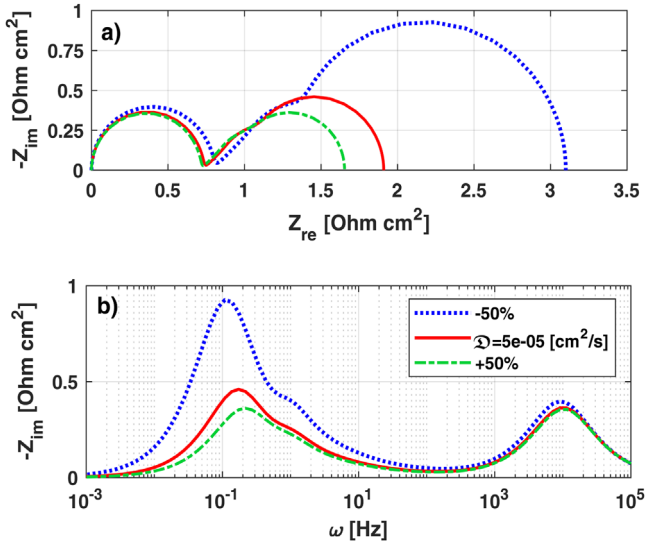

Figure 13. Influence of transport parameter $\mathfrak{D}$ on the Nyquist plot (a) and Bode plot (b).

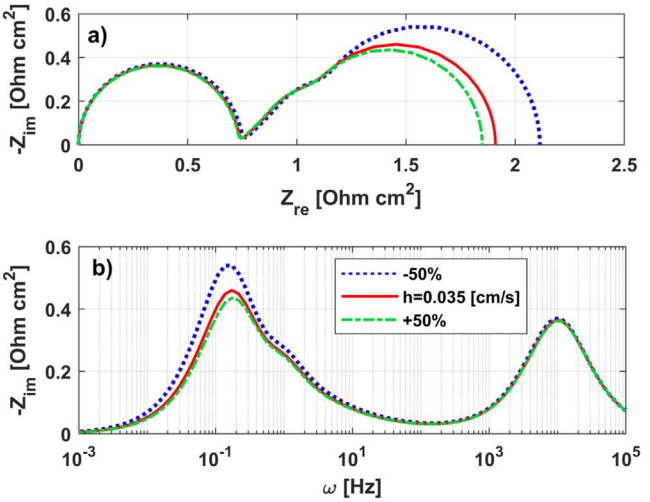

Figure 14. Influence of transport parameter h on the Nyquist plot (a) and Bode plot (b).

reactant distribution within the electrode to become more sluggish and stronger concentration gradients to arise. Figure 13a shows that the low frequency loop of EIS accounts for most of the increase, confirming its strong link to mass transport phenomena.

However, the shape of the second loop is not considerably affected by a change in $\mathfrak{D}$ because the linear and circular feature maintain the same proportions. These results are coherent with what observed in literature.[11,18] The low frequency peak in Fig. 13b responds to a change in $\mathfrak{D}$ with strong shift in frequency. It is observed that a more sluggish mass transport along the through electrode direction causes lower characteristic frequencies. However, a very slow distribution of reactants may cause a reduction in effective length of electrode and can invert the relationship between characteristic frequency of mass transport and $\mathfrak{D}$. In other terms, when ions move slower, electrode starvation along the x direction causes only a narrow part of the electrode to participate to the reaction: despite the decrease in $\mathfrak{D}$, the reduction in effective length causes the characteristic frequency of mass transport to increase.

A.4. Transport coefficient h.—Figure 14 shows the sensitivity of the simulated EIS spectra to a change in h. Higher total resistance derives from lower h as the second loop of EIS becomes more pronounced for lower values of h (see Fig. 14a). The frequency of the low frequency peak in the Bode plot shows weak dependance on h (see Fig. 14b).

A.5. Transport coefficient k.—The transport coefficient k regulates ions transfer from the center of the pore to the active surface of carbon. Sensitivity analysis on k/δ_{BL} is reported in Fig. 15: the Nyquist plots in Fig. 15a are strongly affected by a change in k/δ_{BL}. The effect on the high frequency loop of EIS is minor and is caused by a change in the reactants availability. On the other side, as mass transport to pore active surface becomes more sluggish, the radius of the low frequency loop increases and its shape changes. Specifically, while the circular feature at very low frequencies maintain its shape, the linear feauture elongates and changes its angle. Figure 15c shows the same plot without the curve simulated with a 50% reduction of k/δ_{BL} and better allows to see progressive changes of the linear branch and amplitude of the low frequency feature.The Bode plot displayed in Fig. 15b shows that the charactristic frequency of mass transport does not change with a variable k/δ_{BL}.

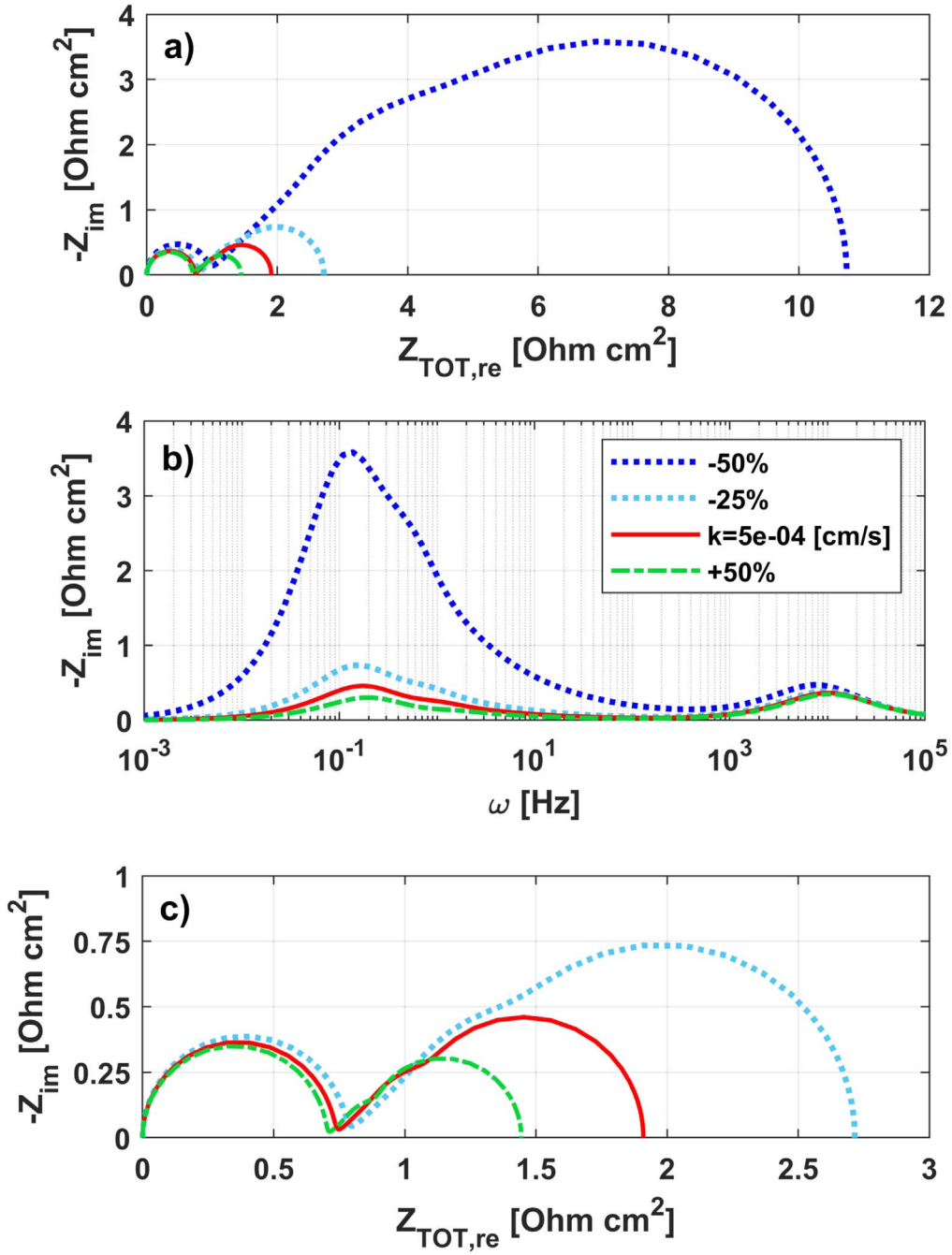

Figure 15. Influence of transport parameter k on the Nyquist plot (a), (c) and Bode plot (b).

Appendix B. Nomenclature

Symbol	
a	Specific surface area (cm^{-1})
b	Tafel slope (V)
c_V	Concentration of vanadium ions (mol cm^{-3})
C_{DL}	Double layer capacitance (F cm^{-3})
$\mathfrak{D}$	Through electrode transport coefficient (cm^2 s^{-1})
E^0	Reversible potential (V)
F	Faraday constant
h	Convective transport coefficient at channel/electrode interface (cm^2 s^{-1})
i	Imaginary unit
j	Current density (A cm^{-2})
k	Transport coefficient to carbon active surface (cm^2 s^{-1})
k_f	Kinetic rate constant of the forward reaction (cm s^{-1})
k_b	Kinetic rate constant of the backward reaction (cm s^{-1})
P	Pressure (Pa)
Pe	Peclet number (−)
r	Spatial coordinate from bulk of electrolyte to carbon active surface (cm)
r_{BV}	Reaction rate (mol cm^{-3})
R	universal gas constant
SoC	State of Charge (−)
t	Time (s)
T	Temperature (K)
V	Potential difference (V)

(Continued).

x	Through electrode spatial coordinate (cm)
Z	Electric impedance (Ω cm^2)
Z_w	Warburg like impedance (−)
Z_{wBL}	Warburg like impedance of boundary layer(−)

Greek

α	Transfer coefficient (−)
δ	Thickness (cm)
η	Overpotential (V)
ϵ^0	Model parameter (−) (19)
ϵ^1_{SoC}	Model parameter (−) (42)
$\epsilon^1_{\Delta\phi}$	Model parameter (−) (43)
λ^0_x	Model parameter (−) (25)
λ_r	Model parameter (−) (40)
λ^1_x	Model parameter (−) (55)
ϕ	Galvani potential (V)
ω	Frequency (Hz)
ω^*	Characteristic frequency (Hz)

Subscript

b	Relative to backward reaction
BL	Relative to boundary layer surrounding the carbon fibers
ch	Relative to flow channel
ct	Relative to charge transfer
el	Measured in the electrolyte
EL	Relative to electrode
f	Relative to forward reaction
im	Imaginary part
mem	Measured at the membrane
ohm	Ohmic
oxi	Relative to oxidation reaction
re	Real part
red	Relative to reduction reaction

Superscript

0	Steady state solution
1	Amplitude of perturbation

ORCID

Daniele Vivona https://orcid.org/0000-0002-1992-0750
Mirko Messaggi https://orcid.org/0000-0002-3447-7224
Andrea Baricci https://orcid.org/0000-0003-2331-7222
Andrea Casalegno https://orcid.org/0000-0002-3396-4979
Matteo Zago https://orcid.org/0000-0002-0542-1459

References

1. C. Zhang, L. Zhang, Y. Ding, S. Peng, X. Guo, Y. Zhao, G. He, and G. Yu, *Energy Storage Mater.*, **15**, 324 (2018).
2. P. Alotto, M. Guarnieri, and F. Moro, *Renew. Sustain. Energy Rev.*, **29**, 325 (2014).
3. A. Z. Weber, M. M. Mench, J. P. Meyers, P. N. Ross, J. T. Gostick, and Q. Liu, *J. Appl. Electrochem.*, **41**, 1137 (2011).
4. V. Viswanathan et al., *J. Power Sources*, **247**, 1040 (2014).
5. B. Zakeri and S. Syri, *Renew. Sustain. Energy Rev.*, **42**, 569 (2015).
6. D. S. Aaron, Q. Liu, Z. Tang, G. M. Grim, A. B. Papandrew, A. Turhan, T. A. Zawodzinski, and M. M. Mench, *J. Power Sources*, **206**, 450 (2012).
7. X. Yuan, H. Wang, J. Colin Sun, and J. Zhang, *Int. J. Hydrogen Energy*, **32**, 4365 (2007).
8. X.-Z. Yuan, C. Song, H. Wang, and J. Zhang, *Electrochemical Impedance Spectroscopy in PEM Fuel Cells* (Springer London, London) p. 1 (2010).
9. R. M. Darling and M. L. Perry, *ECS Transactions*, **53**, 31 (2013).
10. C.-N. Sun, F. M. Delnick, D. S. Aaron, A. B. Papandrew, M. M. Mench, and T. A. Zawodzinski, *ECS Electrochem. Lett.*, **2**, A43 (2013).
11. A. M. Pezeshki, R. L. Sacci, F. M. Delnick, D. S. Aaron, and M. M. Mench, *Electrochim. Acta*, **229**, 261 (2017).
12. C. Sun, F. M. Delnick, D. S. Aaron, A. B. Papandrew, M. M. Mench, and T. A. Zawodzinski, *J. Electrochem. Soc.*, **161**, A981 (2014).
13. L. Wu, J. Wang, Y. Shen, L. Liu, and J. Xi, *Phys. Chem. Chem. Phys.*, **19**, 14708 (2017).
14. I. Derr, M. Bruns, J. Langner, A. Fetyan, J. Melke, and C. Roth, *J. Power Sources*, **325**, 351 (2016).
15. P. Gao, C. Zhang, and G. Wen, *J. Power Sources*, **294**, 67 (2015).
16. M. Eikerling and A. Kornyshev, *J. Electroanal. Chem.*, **475**, 107 (1999).
17. T. E. Springer and I. D. Raistrick, *J. Electrochem. Soc.*, **136**, 1594 (1989).
18. M. Zago and A. Casalegno, *Electrochim. Acta*, **248**, 505 (2017).
19. Q. Xu, T. S. Zhao, and P. K. Leung, *Appl. Energy*, **105**, 47 (2013).
20. M. Al-Yasiri and J. Park, *J. Electrochem. Soc.*, **164**, A1970 (2017).
21. M. Messaggi, P. Canzi, R. Mereu, A. Baricci, F. Inzoli, A. Casalegno, and M. Zago, *Appl. Energy*, **228**, 1057 (2018).
22. K. M. Lisboa, J. Marschewski, N. Ebejer, P. Ruch, R. M. Cotta, B. Michel, and D. Poulikakos, *J. Power Sources*, **359**, 322 (2017).
23. B. Akuzum, Y. C. Alparslan, N. C. Robinson, E. Agar, and E. C. Kumbur, *J. Appl. Electrochem.*, **49**, 551 (2019).
24. Y. Zeng, F. Li, F. Lu, X. Zhou, Y. Yuan, X. Cao, and B. Xiang, *Appl. Energy*, **238**, 435 (2019).
25. A. A. Kulikovsky, *Electrochim. Acta*, **147**, 773 (2014).
26. A. Baricci, M. Zago, and A. Casalegno, *Fuel Cells*, **14**, 926 (2014).
27. A. A. Kulikovsky and M. Eikerling, *J. Electroanal. Chem.*, **691**, 13 (2013).
28. A. A. Kulikovsky, *J. Electrochem. Soc.*, **164**, F379 (2017).
29. T. A. Greszler, D. Caulk, and P. Sinha, *J. Electrochem. Soc.*, **159**, F831 (2012).
30. A. A. Kulikovsky, *Electrochim. Acta*, **225**, 559 (2017).
31. A. A. Kulikovsky, *J. Electrochem. Soc.*, **162**, F217 (2015).
32. A. A. Kulikovsky, *J. Electroanal. Chem.*, **669**, 28 (2012).
33. Y. A. Gandomi, D. S. Aaron, T. A. Zawodzinski, and M. M. Mench, *J. Electrochem. Soc.*, **163**, A5188 (2016).
34. M. Cecchetti, A. Casalegno, and M. Zago, *J. Power Sources*, **400**, 218 (2018).
35. A. A. Kulikovsky, *Analytical Modelling of Fuel Cells* (Elsevier, Amsterdam) p. 1 (2010).
36. Q. Xu and T. S. Zhao, *Prog. Energy Combust. Sci.*, **49**, 40 (2015).
37. J. Houser, J. Clement, A. Pezeshki, and M. M. Mench, *J. Power Sources*, **302**, 369 (2016).
38. C. Liang, H. Koon, and M. Harun, *Electrochim. Acta*, **120**, 167 (2014).
39. X. Ma, H. Zhang, and F. Xing, *Electrochim. Acta*, **58**, 238 (2011).
40. A. A. Shah, M. J. Watt-Smith, and F. C. Walsh, *Electrochim. Acta*, **53**, 8087 (2008).
41. D. Schmal, J. Van Erkel, and P. J. Van Duin, *J. Appl. Electrochem.*, **16**, 422 (1986).
42. N. Pour, D. G. Kwabi, T. Carney, R. M. Darling, M. L. Perry, and Y. Shao-Horn, *J. Phys. Chem. C*, **119**, 5311 (2015).
43. A. A. Kulikovsky, *Electrochim. Acta*, **196**, 231 (2016).
44. J. T. J. Noack, L. Vorhauser, and K. Pinkwart, *ECS Trans.*, **33**, 3 (2011).
45. W. H. Wang and X. D. Wang, *Electrochim. Acta*, **52**, 6755 (2007).
46. D. Manschke, T. Seipp, S. Berthold, and K. A. Friedrich, *Batteries*, **4**, 58 (2018).
47. K. W. Knehr, E. Agar, C. Dennison, and A. R. Kalidindi, *J. Electrochem. Soc.*, **159**, A1446 (2012).
48. A. A. Shah, R. Tangirala, R. Singh, R. G. A. Wills, and F. C. Walsh, *J. Electrochem. Soc.*, **158**, A671 (2011).
49. Q. Xu and T. S. Zhao, *Phys. Chem. Chem. Phys.*, **15**, 10841 (2013).
50. D. Aaron, Z. Tang, A. B. Papandrew, and T. A. Zawodzinski, *J. Appl. Electrochem.*, **41**, 1175 (2011).
51. X. Ke, J. I. D. Alexander, J. M. Prahl, and R. F. Savinell, *J. Power Sources*, **270**, 646 (2014).
52. H. Fink, J. Friedl, and U. Stimming, *J. Phys. Chem. C*, **120**, 15893 (2016).
53. D. Vivona, A. Casalegno, and A. Baricci, *Electrochim. Acta*, **310**, 122 (2019).